Article:
Benkovitz, A, Matthews, A, Teutsch, N et al. (3 more authors) (2020) Tracing water column euxinia in Eastern Mediterranean Sapropels S5 and S7. Chemical Geology, 545. 119627. ISSN 0009-2541

https://doi.org/10.1016/j.chemgeo.2020.119627

Tracing water column euxinia in Eastern Mediterranean Sapropels S5 and S7

Ayelet Benkovitz[1], Alan Matthews[1]*, Nadya Teutsch[2], Simon W. Poulton[3], Miryam Bar-Matthews[2], Ahuva Almogi-Labin[2]

[1] Institute of Earth Sciences, Hebrew University of Jerusalem, 9190401 Jerusalem, Israel

[2] Geological Survey of Israel, 32 Yesha'ayahu Leibowitz St, 9692100, Israel

[3] School of Earth and Environment, University of Leeds, Leeds LS2 9JT, United Kingdom

***Corresponding Author**
Alan Matthews
Fredy and Nadine Herrmann Institute of Earth Sciences
Hebrew University of Jerusalem
Edmond Y. Safra Givat Ram Campus
Jerusalem 9190401, Israel
Email: alan.matthews@mail.huji.ac.il
Mobile +972523244538

Abstract

Sapropels S5 and S7 formed in the semi-enclosed Eastern Mediterranean Sea (EMS) during peak interglacial periods MIS5e and MIS7a, respectively, are considered among the most strongly developed Quaternary sapropels. This study investigates the redox dynamics of the water column during their formation, via Fe isotope and Fe speciation studies of cores taken at 2550 m depth at site ODP-967. Both sapropels show an inverse correlation between $\delta^{56}Fe$ and Fe_T/Al, with slopes mostly matching that found for the Black Sea, pointing to a benthic shelf to basin shuttle of Fe and subsequent precipitation of Fe sulphides in euxinic bottom waters. An exception to these Black Sea-type trends occurs during the later, peak, stages of S7, where the negative $\delta^{56}Fe$ - Fe_T/Al slope shallows. Fe speciation studies reveal that the dominant highly reactive Fe phase (Fe_{HR}) in the sapropels is pyrite, with Fe (oxyhydr)oxides forming the second major mineral component. Correspondingly, Fe_{HR}/Fe_T plots show increased strengthening of anoxic water conditions during the passage from pre-sapropel sediment into the sapropel. Nevertheless, despite the evidence for euxinic conditions from both Fe isotopes and high Mo concentrations in the sapropel, Fe_{py}/Fe_{HR} ratios remain below values commonly used to identify water column euxinia. This apparent contradiction is ascribed to the sedimentary preservation of a high flux of crystalline Fe (oxyhydr)oxide minerals to the basin, which resulted in a relatively low degree of sulphidation, despite the presence of euxinic bottom waters. Thus, the operationally defined ferruginous/euxinic boundary for EMS sapropels is better placed at $Fe_{py}/Fe_{HR} = 0.6$, which is somewhat below the usually ascribed lower limit of 0.7. Consistent with the significant presence of crystalline Fe (oxyhydr)oxides, the change in the $\delta^{56}Fe$ - Fe_T/Al slope during peak S7 is ascribed to an enhanced monsoon-driven flux of detrital Fe(III) oxides from the River Nile into the EMS basin and comcomitant diagenetic sulphidation. Euxinic water column conditions in sapropel S5 and S7 are interpreted here to reflect the positive balance between dissolved sulphide formation and rates of reductive dissolution of Fe (oxyhydr)oxide minerals. Both of these parameters in turn depend on the extent to which water overturn times are reduced and export productivity increased during sapropel formation.

Keywords: Fe isotopes, Fe speciation, organic-carbon–rich sedimentation, Sapropels S5 and S7, Eastern Mediterranean Sea, benthic Fe isotope shuttle, water column euxinia, sulphidation, ferruginous-euxinic Fe_{py}/Fe_{HR} boundary, authigenic Fe mineral deposition dynamics

1 Introduction

Mediterranean sapropels are organic carbon-rich sediments and are important for the understanding of water column redox conditions in low-oxygen environments. Their late Quaternary formation and good preservation in cores makes them excellent proxies for recording sedimentation and early diagenesis of organic carbon-rich sediments. Sapropels provide insights that bridge the gap between modern day deposits, such as the Black Sea, and consolidated sediments in Phanerozoic and more ancient rocks. Moreover, sapropels formed during reduced oxygen conditions related to global and regional climatic forcing events. Two major processes are proposed to account for the formation and preservation of organic matter in sapropels: (1) higher export productivity, which generates anoxicity through the consumption of oxygen and (2) physical disruption of the normal thermohaline water overturn system, leading to bottom water stagnation (Rossignol-Strick et al., 1982; Rohling and Hilgen, 1991; Calvert et al., 1992; Rohling, 1994; Thomson et al., 1999; Weldeab et al, 2003; Meyers, 2006; de Lange et al., 2008; Meyer and Kump, 2008). In the Eastern Mediterranean Sea (EMS), physical disruption of water overturn is related to freshening of the sea surface layer during enhanced insolation-driven (precession cycle) riverine discharge, primarily that of the River Nile, and amplified rainfall (Rossignol-Strick, 1985; Emeis et al, 1998; Emeis et al., 2003; Scrivner et al., 2004; Osborne et al., 2008; Bar-Matthews, 2014; Rohling et al., 2015; Wu et al., 2018). Coupled oceanographic-biogeochemical models also stress the potential importance of anoxic deep water formation resulting from sea level rise following glaciation (Grimm et al., 2015; Grant et al., 2016). U-Mo isotope study of sapropel S5 formed during the last interglacial MIS5e-indicates that deep water overturning circulation in the EMS (Fig. 1) could have decreased by a factor of 10 (Andersen et al., 2018).

Oxygen depleted water conditions show considerable variation during sapropel deposition. de Lange et al. (2008) demonstrated the regional-scale presence of anoxic bottom waters at depths >1800 metres below sea level (mbsl) during EMS Holocene sapropel S1. A recent Nd isotope study of water circulation dynamics shows that stagnant conditions prevailed at depths > 800 mbsl throughout the entire Mediterranean basin (Wu et al., 2019). Sub-oxic bottom water conditions were identified in S1 sediment recovered at 1780 mbsl water depth in the EMS eastern Levantine basin, (Tachikawa et al., 2015). S1 sapropels deposited in the Nile Fan at sub-oxic to anoxic conditions show absence of benthic foraminifera, together with

evidence for enhanced Nile suspended sediment flux, pollen and spore transport (Almogi-Labin et al., 2009; Box et al., 2011; Langgut et al, 2011; Revel et al., 2014; Hennekam et al., 2015; van Helmond et al., 2015; Matthews et al., 2017). Euxinic (sulphidic) water column conditions are less commonly identified for the S1 event. Azrieli-Tal et al. (2014) used Mo/U systematics and Mo and Fe stable isotope compositions to infer weakly sulphidic bottom water conditions for S1 sediments taken from ODP Leg 160 core 967D at 2550 mbsl (Fig. 1). Fillipidi and de Lange (2019) deduced sulphidic water conditions below 1400 mbsl from a bathymetric transect of S1 at the transition between the Adriatic Sea and the EMS.

In contrast to S1, Pleistocene sapropels S5 and S7 are among the most intensely developed of the more recent sapropels (Rohling et al., 2006; Gallego-Torres et al., 2010; Melki et al., 2010) and the most likely to record euxinia. Rohling et al. (2006) proposed photic zone euxinia during S5 based on the presence of green sulphur bacteria (isorenieratene) at ODP site 971 (western Levantine basin, south of Crete; 2026 mbsl). Rohling et al. (2015) further proposed a model for S5 formation in the EMS featuring photic-zone euxinia in the Aegean, Ionian and western Levantine sub-basins and a basin wide anoxic sea floor 'blanket' overlying the surface topography. Nijenhaus et al. (1999) and Passier et al. (1999a) also inferred regional sulphidic water conditions in Leg 160 Pliocene sapropels on the basis of the presence of isorenieratene derivatives and high trace element scavenging.

Numerous geochemical proxies have been used to interpret redox conditions prevailing prior to, after, and during sapropel formation, including: $\delta^{18}O$ of planktonic and benthonic foraminifera, organic biomarkers, elements sensitive to paleoproductivity and organic burial (e.g. Ba, Ni) and reduction sensitive trace elements (RSTE: Mo, U, V), S isotopes, Sr and Nd isotopes (e.g., Passier et al., 1996; van Santvoort et al., 1996; Thomson et al., 1999; Warning and Brumsack, 2000; Cane et al., 2002; Rohling et al., 2006; de Lange et al., 2008; Almogi –Labin et al., 2009; Gallego-Torres et al, 2010; Wu et al., 2019)). Redox sensitive metal stable isotopes (Mo, Fe, U) are among the newer proxies providing new insights into water column conditions (Reitz et al., 2007; Scheiderich et al., 2010; Azrieli-Tal et al., 2014; Matthews et., 2017; Andersen et al., 2018). The transition metal isotope systems of Mo and Fe are powerful tracers of redox conditions in the water column and pore waters (Arnold et al., 2004; Neubert et al., 2008; Johnson et al., 2008; Kendall et al.,

2016; Dauphas et al., 2016). Sediments acquire high Mo contents and the Mo isotopic signature of seawater ($\delta^{98/95}$Mo ~2.3‰) in euxinic water conditions due to quantitative Mo scavenging (Arnold et al., 2004; Neubert et al., 2008; Nägler et al., (2011). Recent experimental and thermodynamic modeling studies suggest that Mo uptake into euxinic sediments likely reflects increasing bottom water sulphide concentrations, which initiates the reversible precipitation of $FeMo(VI)S_4$, followed by its irreversible transformation to $FeMo(IV)S_2(S_2)$ (Helz et al., 2011; Vorlicek et al., 2018; Helz and Vorlicek, 2019). The effects of water column sulphide formation are particularly evident in the Fe isotope system, where a major diagnostic feature is an inverse correlation between δ^{56}Fe and Fe_T/Al during euxinic sedimentation. This inverse relationship reflects the benthic shelf to euxinic basin export of isotopically light $Fe(II)_{aq}$ and subsequent precipitation and sedimentation of Fe sulphides (Severmann et al., 2008; Lyons et al., 2009; Severmann et al., 2010).

Fe speciation studies complement stable metal isotope as tracers of water redox conditions. The sequential Fe speciation studies, as developed by Poulton and Canfield (2005); reviewed by Poulton and Canfield (2011) and Raiswell et al. (2018), provide a measure of highly reactive Fe (Fe_{HR}), which refers to Fe minerals that are considered highly reactive towards biological/abiological reduction under anoxic conditions (Canfield et al., 1992; Canfield et al., 1996; Raiswell and Canfield, 1998; Poulton et al., 2004). Fe speciation studies, involving a series of sequential dissolution steps, measure distinct mineralogical fractions such as Fe (oxyhydr)oxides (Fe_{ox}), magnetite (Fe_{mag}) and pyrite (Fe_{py}); allowing distinction between oxic and anoxic water column conditions and between euxinic and ferruginous conditions in anoxic waters (Poulton and Canfield, 2011).

This study uses Fe isotope and Fe speciation in combination with selected RTSE measurements to investigate water column redox conditions during the formation of sapropel S5 (hereafter "S5") and sapropel S7 (hereafter "S7"), deposited in EMS deep waters at ODP site 967 (Fig 1). Both sapropels formed at peak interglacial periods characterized by strong insolation maxima, MIS5e and MIS7a, respectively (Fig. 1). Fe isotope and Fe speciation methods enable specific focus on the development of water column euxinia during sapropel formation, the mechanisms of authigenic Fe sulphide formation, and the controls of anoxic water column formation. An important wider implication of the Fe speciation studies in this paper is

that the operationally defined ferruginous/euxinic boundary for EMS sapropels is placed at lower limit than usually ascribed to consolidated sediments of the past.

Currently accepted models of Fe mobilization in sapropels favour diagenetic processes in which pyrite formation within and directly below sapropels is governed by the relative rates of sulphide production and Fe release and diffusion (Passier et al., 1996; Passier et al., 1997; Passier et al., 1999b). These studies envisaged two contrasting models of pyrite formation: (1) 'high Fe content model: sulphide production is lower than Fe liberation and supply; (2) 'low Fe content' model: excess sulphide production leads to its migration into the underlying sediments and bottom waters. In the former scenario, reduced S is fixed as pyrite by reaction with Fe(oxyhydr)oxides and upward diffusing Fe(II) liberated from the underlying sediments. In the latter scenario, pyrite formation is fixed within the sapropel; upward diffusing Fe(II) does not reach the sapropel, but reacts to form pyrite with downward migrating sulphide, which also sulphidizes Fe oxides below the sapropel. These well-developed models present an opportunity to examine between diagenetic Fe mobilization and the water column proxies studied in this work.

2. Samples and Methods

The samples were taken from cores drilled at ODP site 967, located at 2550 m depth in the Cyprus Arc on the northern lower flanks of the Eratosthenes Sea mount (Fig. 1b). Bulk sample profiles were taken of both sapropels (1-2 cm intervals) and enclosing sediments (1-5 cm intervals) from core sections 967C-1H5 (S5) and 967D-2H2,3 acquired from the IODP Core Depository, Bremen. S5 samples were obtained by resampling the S5 core section studied by Scrivener et al. (2004),Vance et al. (2004), and Andersen et al (2018). The received core samples were subdivided into two portions; one portion was taken for Fe isotope and Fe speciation studies and the second portion for chemical analytical work. The wet samples were freeze dried using a lyophilizer and stored in closed vials prior to the analytical work.

Sample preparation and measurements were conducted at the facilities of the Hebrew University, Israel (clean laboratory chromatographic Fe separation), the Geological Survey of Israel (Fe isotopes, trace and major element chemistry), and the University of Leeds (Fe speciation).

2.1

Major and trace metal chemistry and analyses

Organic matter was content was determined by low temperature plasma ashing of weighed amounts of sediments. Chemical analyses were made at the Geological Survey of Israel (GSI) using sodium peroxide sintered solution for S7 samples and HF-HNO_3-HCl digested solution for S5 samples. Major elements were analysed by ICP-OES and trace elements by ICP-MS as reported in Azrieli-Tal et al. (2014). Based on the analyses of geostandards BHVO-1 and GIT-IWG IF-G (supplement 1), analytical errors on single values for major and trace elements using both procedures were within ±5%.

2.2.

Fe isotope analyses

Digestion of samples for Fe separation and isotopic analysis was done in the clean laboratory at the Hebrew University of Jerusalem (HUJI). Samples were pyrolized at 800°C for approximately 12 hours to oxidize organic carbon. The pyrolized residue was then dissolved using HF, HNO_3 and HCl in the presence of H_2O_2. Iron isotope analyses were measured on a Nu Plasma II MC-ICP-MS at GSI, using the sample-standard bracketing approach in medium resolution mode. Iron purification was based on the protocol developed at ETH, Zurich (Teutsch et al., 2005). Details of these procedures and standard calibrations are given in Supplement 2.

The δ^{56}Fe values are reported relative to the IRMM-014 metal standard. Results for repeated δ^{56}Fe measurements of the ETH Fe-salt solution standard (over 18 months) are −0.73±0.11‰ (2 SD, n=61), which is identical within errors to previously published data (−0.71±0.18‰, Teutsch et al., 2009 and −0.73±0.10‰, Fehr et al., 2008). The geochemical reference sample, IF-G, processed in four different sessions (including digestion and column chemistry) produced δ^{56}Fe = 0.63±0.09‰ (2 SD, n=16), which is in excellent agreement with the recommended value of 0.639±0.013‰ (Craddock and Dauphas, 2011 and references cited therein). Duplicates of 2 samples were fully processed including column chemistry to check for reproducibility. Results on both Fe solutions after column chemistry are within instrumental error (Supplement 2).

All published δ^{56}Fe analyses cited relative to the Madison igneous rock standard (Beard et al., 2003a) are adjusted in this paper to the IRMM-014 standard.

Data reported using $\delta^{57}Fe$ IRMM-014 values (Azrieli-Tal et al., 2014) are recalculated to $\delta^{56}Fe$ values using the mass fractionation relationship. Isotopic fractionation factors are expressed as $\Delta^{56}Fe_{A-B} = \delta^{56}Fe_A - \delta^{56}Fe_B$.

2.3

Fe speciation measurements

Fe extractions were made on bulk samples at the University of Leeds using the calibrated extraction of Poulton and Canfield (2005), as modified for application to recent sediments (see Goldberg et al., 2012; Zegeye et al., 2012; Matthews et al., 2017; Xiong et al., 2019). The first step consists of a 0.5 N HCl extraction for 1 h, which targets reduced Fe phases, including acid volatile Fe sulphides (Fe_{AVS}) such as mackinawite, surface-reduced Fe(II), and potentially some poorly crystalline ferrous carbonate/phosphate phases. The Fe_{AVS} is also measured separately (see below), and thus after subtraction of Fe_{AVS}, this pool consists of the remaining non-sulphidized Fe(II) minerals (termed $Fe(II)_{HCl}$). The $Fe(II)_{HCl}$ pool was determined by spectrophotometer using the ferrozine assay (Stookey, 1970), immediately after completion of the extraction. The 0.5 N HCl extraction also extracts the most reactive Fe(III) minerals remaining in the sediment, in particular ferrihydrite (termed $Fe(III)_{HCl}$). This pool was determined by atomic adsorption spectrometry (AAS), after subtraction of $Fe(II)_{HCl}$ and Fe_{AVS}. The second sequential extraction step utilizes a buffered Na dithionite solution to extract more crystalline Fe (oxyhydr)oxide minerals, such as goethite and hematite (termed Fe_{ox}; Poulton and Canfield, 2005). The final sequential extraction targets magnetite, using a Na oxalate extraction (termed Fe_{mag}; Poulton and Canfield, 2005). The Fe_{ox} and Fe_{mag} fractions were measured via AAS, with all sequential extraction steps giving a RSD of <5%, based on replicate extractions. Total Fe (Fe_T) values were determined via an HF-$HClO_4$-HNO_3 extraction on ashed sediments, followed by analysis by AAS. Replicate extractions of international sediment standard PACS-2 gave a RSD of 2% and a recovery of 98% for Fe.

Pyrite (Fe_{py}) and Fe_{AVS} were determined via the procedure of Canfield et al. (1986), whereby Fe_{AVS} is extracted using hot 6 N HCl, and Fe_{py} is extracted from the residue via chromous chloride distillation. These determinations indicated that Fe_{AVS} was below detection in all cases. The H_2S liberated by chromous chloride distillation was precipitated as Ag_2S, and sulphide was determined gravimetrically and then

converted to Fe concentrations according to the stoichiometry of the mineral phase (i.e., as FeS_2 for pyrite). Replicate extractions gave a RSD of <5% for the sulphide extraction. The sum of $Fe(II)_{HCl}$, $Fe(III)_{HCl}$, Fe_{ox}, Fe_{mag}, and Fe_{py} defines the Fe_{HR} pool.

Table 1 lists sample depths, isotopic data, and elemental proxies used in this study. The elemental data are normalized to Al to minimize the effects of fluctuations in carbonate or silica-bearing biogenic sediment content (Thomson et al., 1999; Raiswell et al., 2018), with the exception of TOC. A complete listing of bulk sample chemical analyses is given in Supplement 1. As noted, Supplement 2 details Fe isotope procedures and standard calibrations. Fe speciation data are presented in Supplement 3. Supplement 4 presents calculations of detrital and authigenic U, Mo, Fe elemental fractions and authigenic Fe isotopic compositions.

3. Results

3.1

Sapropel boundaries and timing.

Establishing the upper and lower boundaries between sapropels and their underlying (pre-sapropel) and overlying (post-sapropel) sediments is most commonly done using a combination of Ba/Al (a paleoproductivity proxy; Thomson et al., 1999; Weldeab et al., 2003) and total organic carbon (TOC) core depth profiles. Using both proxies avoids incorrect boundary assignment due to post-sapropel organic matter oxidation (burndown), which may truncate the TOC profile. In the case of S5 and S7 at ODP site 967 (hereafter "ODP967"), the boundaries defined by both Ba/Al and TOC enrichments coincide (S5: Fig. 2A; S7: Fig. 2B), indicating that oxidative burndown was negligible. The lower and upper sapropel boundaries at 103.5 and 74 cm (S5) and 154.5 and 131.5 cm (S7) indicate that the sapropels have thicknesses of 29.5 and 23 cm, respectively. Ni/Al has also been recognized as a potential paleoproductivity proxy (Tribollivard et al., 2006) and its elevated values in the sapropels are compatible with this boundary definition (Figs. 2A, 2B). Nevertheless, the Ni/Al profiles are sufficiently similar to the other RSTE profiles, that it is not possible to distinguish a unique productivity signal. Mn/Al profiles are also a useful indicator of reduced oxygen (sub-oxic) conditions and frequently show peaks at sapropel upper and/or lower boundaries (van Santwoort et al., 1996; Thomson et al.,

1999; de Lange et al., 2008). The Mn/Al profile of S5 shows both peaks, whereas S7 only shows the lower boundary peak (Figs. 2A, 2B). The latter is generally interpreted as reflecting mobilization of Mn in anoxic sapropel and its re-precipitation at the interface between the organic-rich sediment and the underlying sediment (van Santvoort et al., 1996).

The duration of S5 at ODP967 has been independently estimated as 6.8 ky from 128.3 to 121.5 ka (Grant et al., 2012 (Fig. 1). Assigning an accurate age to S7 is more problematic. Emeis et al. (2003) estimated a 6 ky timespan at ODP 967 from 197 to 191 ka, based on tuning the sapropel onset to peak insolation. This timescale broadly matches the timing of a syn-S7 rainfall event recorded in the EM speleothem record (Bar-Matthews et al., 2003). However, based on constant linear sedimentation rates between adjacent sapropels and 21 ky insolation cycles, Gallego-Torres et al. (2010) showed that S7 could have formed between *ca* 200 to 189 ka at ODP site 966 (located 25 km south of ODP967 on the northern Erastothenes Seamount plateau). Here, we report all our time series data according to core depth in cm (Table 1). For reference, the sapropel durations of Grant et al. (2012) for S5 and Emeis et al. (2003) for S7 are plotted at the top of Figs. 2A and 2B.

3.2

Geochemical proxies for redox conditions

3.2.1

Fe_T/Al variations

Fe_T/Al ratios show enrichments in both S5 and S7 relative to background sediment values (Fig. 2). At its onset and for the first ten cm, S5 shows a moderate overall rise (Fe_T/Al < 1) from initial sediment Fe_T/Al values, but there is then a marked rise to Fe_T/Al =1.3 at 92.5cm, followed by elevated Fe_T/Al values of 1.0-1.25 for the rest of the sapropel until its termination at 74 cm (Fig 2A). These trends match those previously found for the <63 mm fraction of the same core section of S5 (Andersen et al., 2018). S7 initially behaves similarly to S5 with moderate of Fe_T/Al values in the first 10 cm, but there is then a rapid rise to values greater than 1.5 at 140.5-137.5 cm, reaching a maximum Fe_T/Al of 1.9 at 137.5 cm (Fig 2B). Following this peak there is a smooth well defined decrease in Fe_T/Al values until termination of the sapropel at 131.5 cm.

A significant feature of the sediments enclosing both sapropels is their high background Fe_T/Al values (0.62-0.83), which overlap and exceed the upper limit of

the range of 0.55 ± 0.11 defined for modern marine sediments deposited under oxic conditions (Clarkson et al., 2014). Similar high background sediment Fe_T/Al values were also observed in other EMS sapropel sites (sapropel S1from ODP967 and cores MD9501 and MD9509; Fig. 1) and reflect a very high detrital Fe mineral input from the River Nile into the EMS (Poulton and Raiswell, 2002; Lyons and Severmann, 2006; Matthews et al., 2017). The average Fe_T/Al value of non-sapropel sediments sampled at ODP 967 is 0.724 ± 0.064; 1SD; n=35; Supplement 4).

3.2.2

Authigenic U–Mo enrichments

Redox sensitive trace element (RSTE) proxies U/Al, V/Al and Mo/Al (Figs. 2A, 2B) show marked enrichments in both sapropels, which broadly match the Fe_T/Al profiles. Late sapropel peaking of RSTE was also found at nearby ODP site 966 (Gallego-Torres et al., 2010). Commonly adopted schemes for estimating the authigenic elemental fractions use the measured element abundances compared to [Al], and normalize these ratios to the estimates from detrital terrigenous siliciclastics, giving relative authigenic enrichment factors (EF) (e.g. Warning and Brumsack, 2000, Brumsack, 2006; Algeo and Tribovillard, 2009). Elevated EF estimates for [U] and [Mo] (Table 1) indicate that the authigenic fraction (>95%; Supplement 4) dominates both the Mo and U budgets during the sapropel events. The sediments surrounding S5 and S7 tend to have relatively higher U_{EF} compared to Mo_{EF} (Fig. 3). Comparing the background sediment values to the schematic marine water mass trajectories of Algeo and Tribovillard (2009), gives a broad trajectory from open marine anoxic to progressively more sulphidic conditions (trends 2 and 3), with elevated Mo_{EF} over U_{EF}. The sapropels deviate from this trend and plot close to the Mo/U seawater line (Fig. 3). These seawater Mo_{EF} to U_{EF} trends in S5 and S7 also differ from those of Black Sea sediments, which show a flatter trajectory (high enrichment factors with elevated U_{EF} over Mo_{EF}) that reflect Mo depletion in a highly restricted basin (Fig. 3). Algeo and Tribollivard (2009) suggest that the sapropel-type trajectory could occur when the tendency toward higher $(Mo/U)_{EF}$ values under reducing (sulphidic) conditions was offset by lower aqueous Mo concentrations in a moderately restricted basin. This would be consistent with the much larger size and sill-restricted surface water inflow/outflow conditions of the EMS (Fig. 1).

The Mo_{EF}/U_{EF} trajectory of S7 differs from that of S5 in one significant respect. This is the gradual decline in $(Mo/U)_{EF}$ values from the seawater trend shown

by the uppermost 4 samples of the sapropel (136.5-131.5 cm) (Fig. 3), which is not observed in S5 samples. The progressive decline in enrichment factors in these uppermost samples correlates with sample depth. The slope of the S7 decline broadly parallels the sulphidic-anoxic trends 2 and 3, suggesting a progressive, rather than abrupt, transformation from sulphidic through to anoxic non-sulphidic conditions.

3.3.

Fe isotope profiles

Fe_T/Al and δ^{56}Fe profiles indicate opposed enrichment/depletion relationships between the two proxies (Fig. 4). Background sediment Fe_T/Al ratios correspond to δ^{56}Fe values that generally fall within the 0 to 0.2‰ range typical of igneous minerals, suspended river sediments and marine sediments (Beard et al., 2003b; Severmann et al., 2008; Escoube et al., 2009; Poitrasson et al., 2014). Exceptions to this general trend are three samples of pre-S5 sediment at 126.5 to 116.5 cm, which have high δ^{56}Fe values of 0.3 to 0.5‰. Sapropel δ^{56}Fe values are mostly negative, the few exceptions being samples that also have Fe_T/Al values close to the background sediment range of 0.72 ± 0.07. The most negative δ^{56}Fe value in S5 (-0.72‰) matches the Fe_T/Al peak of 1.31 at 92.5 cm, whereas the remaining sapropel shows δ^{56}Fe values of -0.2 to -0.6‰, corresponding to Fe_T/Al values of 1.0 to 1.2 (Fig. 4a). As with S5, the first ten cm of sapropel S7 are mostly characterized by moderate Fe_T/Al enrichments and slightly negative δ^{56}Fe values, but where Fe_T/Al shows a sharp rise at 145 cm, a commensurate drop occurs in δ^{56}Fe. The most negative δ^{56}Fe values (-0.7 to -0.4‰) occur when Fe_T/Al values exceed 1.2, and there is a gradual rise in δ^{56}Fe during the terminal decay of the sapropel.

3.4

Fe speciation mineralogy,

The five Fe_{HR} fractions extracted by the Fe speciation measurements (Supplement 3), represent: (1) $FeII_{HCl}$- surface reduced Fe(II) and potentially poorly crystalline ferrous carbonate/phosphate minerals (i.e., unsulphidized Fe(II); (2) $Fe(III)_{HCl}$ -ferrihydrite, a likely oxidation product of AVS and pyrite; (3) Fe_{ox} – ferric (oxyhydr)oxides (hematite/goethite); (4) Fe_{mag} – magnetite; and (5) Fe_{py} – pyrite. Ferrihydrite is considered an unlikely primary mineral phase in sulphidic sapropel sediments due to the rapid sulphidation kinetics of this phase (Poulton et al., 2004), and the $Fe(III)_{HCl}$ fraction in these core samples (which were not stored anoxically)

most likely represents the oxidation product of AVS and pyrite. Accordingly, the $Fe(III)_{HCl}$ pool is added to the Fe_{py} fraction to give an estimate of the total Fe sulphide pool prior to post-sampling oxidation. Following Matthews et al. (2017), this pyrite dominated Fe sulphide pool is referred to as $CorrFe_{py,}$. Pyrite is taken to be the predominant mineral phase though the presence of minor amounts of FeS minerals would not affect the conclusions of this paper.

The Fe-speciation profiles (Fig. 5) show that pyrite is the major Fe_{HR} mineral phase in both sapropels and pre-sapropel sediments. The second major component is crystalline Fe (oxyhydr)oxides (Fe_{ox}), which, however, become more abundant than pyrite in post-sapropel sediments. Fe_{mag} and $Fe(II)_{HCl}$ are minor components of Fe_{HR} (<0.4 wt%) in both sapropels (Fig. 5). Pyrite abundances broadly match the enrichments in Fe_T/Al and depletions in $\delta^{56}Fe$ (Fig. 4), suggesting that pyrite is a major carrier of both of these signatures. Notably, crystalline Fe (oxyhydr)oxides do not show a significant decrease in the sapropels relative to the background sediments (see Matthews et al. (2017) for an opposite case where diagenetic reactions in Sapropel S1 leads to pyrite replacing Fe (oxyhydr)oxides). Rather, with the exception of five samples in S7 (141.5-137.5 cm), Fe_{ox} values are relatively constant in both sediments and sapropels (0.64 ± 0.16 wt%, 1SD). The five exceptional Fe_{ox} values show correlated increases in both Fe_{ox} and $CorrFe_{py}$ (and Fe_{HR}) (Fig. 5), though the relative increase in Fe_{ox} (0.84 to 1.8 wt%) is greater than that of $CorrFe_{py}$ (3 to 3.5 wt%). These high Fe_{ox} values correspond to 16-25% of the total Fe in the sapropel.

The inorganic redox aspects of the dominant pyrite and Fe (oxyhydr)oxide mineral phases are readily evident from classic Eh-pH diagrams in the system Fe-O-H-S (e.g., Langmuir, 1997, Chapter 12). At pH values of ~7-8, which are appropriate to euxinic marine settings (Helz et al., 2011; Kondratev et al., 2017), hematite or goethite would be the stable Fe minerals over a wide range of Eh values. Only in the most reducing conditions would pyrite become the stable mineral. The stable formation of authigenic pyrite in euxinic bottom waters therefore renders Fe (oxyhydr)oxides to be metastable minerals, be they of detrital or authigenic origin. In sulphide-free waters, magnetite or siderite would occupy the reducing field occupied by pyrite, as is commonly found in anoxic Precambrian marine settings where sulphate (and hence porewater sulphide) was much lower than the present day (Canfield et al., 2008; Poulton et al., 2010; Raiswell et al., 2011).

4. Discussion

4.1

Shelf to basin Fe transport during sapropel formation

4.1.1

Benthic Fe shuttle

$\delta^{56}Fe$ values and Fe_T/Al ratios values (Fig. 4) are diagnostic parameters of the benthic iron shuttle model (Canfield et al., 1996; Wijsman et al, 2001; Lyons and Severmann, 2006; Severmann et al., 2008; Severmann et al., 2010; Raiswell and Canfield, 2012). A key feature of this model is an inverse correlation between Fe_T/Al and $\delta^{56}Fe$, which has been recognized in modern euxinic basins such as the Black Sea and the Baltic Sea (Severmann et al., 2008; Fehr et al., 2008, 2010; Wegwerth et al., 2018). The benthic Fe shuttle model envisages onlapping of the sub-oxic chemocline waters onto the continental shelf (Raiswell and Canfield, 2012). The inverse correlation represents the remobilization of Fe from shelf porewaters and its shuttling as isotopically depleted $Fe(II)_{aq}$ into euxinic basin bottom waters, where reaction with dissolved sulphide gives rise to isotopically light authigenic pyrite. This diagnostic feature was identified in sapropel S1 at ODP 967D (Azrieli-Tal et al., 2014), but is not present in sapropel S1 in the Nile Fan, where pyrite was formed by diagenetic porewater reactions (Matthews et al., 2017).

As originally described for the Black Sea by Severmann et al. (2008), the Fe sources for the shuttle were oxic shelf sediments with Fe_T/Al values 0.4 to 0.6 (i.e., within the modern oxic range of 0.55 ± 0.11; Clarkson et al., 2014). This range is significantly lower than the average background sediment Fe_T/Al of 0.73 ± 0.07 at ODP 967. Indeed, background sediments at intermediate depth (~900 m) core sites MD9509 and MD9501in the Nile Fan (Fig.1) have even higher Fe/Al values of 0.79 ± 0.02 (1SD; n=15), directly reflecting the high Fe content of the suspended load output from the Blue Nile (Supplement 4). Given these high background sediment Fe_T/Al values, an offset from the original Black Sea benthic Fe_T/Al-$\delta^{56}Fe$ trend is anticipated.

Both S5 and S7 show inverse correlations between Fe_T/Al and $\delta^{56}Fe$ (Fig. 6). The shifts in Fe_T/Al and $\delta^{56}Fe$ initiate at the lower sapropel boundary (Fig. 4) and indicate that the shuttle commences at the sapropel onset. These inverse correlations are displaced to higher Fe_T/Al values in comparison to the Black Sea, but nonetheless,

the Fe_T/Al vs δ^{56}Fe trend for S5 and most of the S7 samples falls parallel to that identified by Severmann et al. (2008) for the Black Sea (Fig. 6), and are significantly steeper in slope than that previously found for the weakly euxinic sapropel S1 at ODP967 (Azrieli-Tal et al., 2014). However, whereas most sapropel S7 samples fit the Black Sea trend, there is a clearly defined flattening of the trend at high Fe values. This flattening is exhibited by the previously noted samples with peak Fe_T/Al values at 141.5 to 137.5 cm. Thus, the overall S7 trend is best described by two segments, one subparallel to the Black sea trend, the second (defined by the five samples) by a shallow, almost horizontal slope (Fig. 6). Overall, however, the data strongly support the Severmann et al. (2008) benthic Fe isotopic model for shuttling of isotopically light Fe(II) into strongly euxinic bottom waters, with a substantial part of the light isotopic signatures being derived from the abundant pyrite (Fig. 5). Nevertheless, questions remain as to the reasons for the five 'anomalous' samples at the peak of S7. This question will be developed further in the next section via consideration of authigenic vs detrital inputs to the EMS.

4.1.2

Authigenic Fe transport into EMS deep water

Fe_T/Al enrichments and δ^{56}Fe depletions reflect authigenic Fe transported into the euxinic basin by the iron shuttle. The authigenic Fe fraction (Fe_{auth}) and its Fe isotopic composition ($\delta^{56}Fe_{auth}$) can be estimated with a simple two-end member mixing model from the elemental concentrations and bulk δ^{56}Fe values, as done for U and Mo by Andersen et al. (2018) and for Fe by Severmann et al. (2008, supplementary data). The mass balance calculations require the determination of Fe_T/Al ratios and δ^{56}Fe values of the detrital Fe fraction (Fe_{det}). These are taken as the average values for background sediments: Fe_T/Al = 0.724 (n=35) and δ^{56}Fe = 0.15‰ (n=14). The detrital Fe (Fe_{det}) wt% in a sapropel sample is then calculated from its Fe_T/Al value, and the authigenic Fe wt% given by subtraction of Fe_{det} wt% from the bulk sample Fe wt%. The authigenic calculations (including those mentioned earlier for U and Mo) are given in Supplement 4. Percentage Fe_{auth} values of the sapropels are detailed in Table 2, and vary from 15% in samples with lowest Fe_T/Al values, up to 60%. The Fe_{auth} percentage is significantly lower than the authigenic Mo and U estimates for the sapropel samples (>90%), reflecting the modal importance of the detrital Fe component in the sapropel sediment, compared to the chemically

precipitated RSTE. Corresponding $\delta^{56}Fe_{auth}$ values are calculated from Fe_{auth} fractions and bulk $\delta^{56}Fe$ values by subtracting the detrital contribution and detrital $\delta^{56}Fe$ value (Supplement 4). Uncertainties in this composition are propagated from $\delta^{56}Fe$ errors (Table 1) by weighting the relative size of the detrital component (Andersen et al., 2014, 2018). The authigenic calculations are only made for sapropels with Fe_T/Al values > 0.86, i.e., with Fe_T/Al at least 2SD higher than the detrital Fe_T/Al value. Even so, sapropels with low Fe_T/Al values (<1) and higher bulk sample $\delta^{56}Fe$ show significant errors (Table 2 and Fig. 7).

The calculated $\delta^{56}Fe_{auth}$ averages at -1.33 ± 0.51‰ (S5) and -1.22 ± 0.24‰ (S7). These numbers compare with $\delta^{56}Fe_{auth}$ values of -1.4 ± 0.3‰ estimated for Black Sea euxinic sediments (Severmann et al., 2008). Assuming that the Fe_{det} fraction mainly consists of Fe (oxyhydr)oxides, minor magnetite and Fe-silicate minerals, then it is clear that the negative isotope Fe_{auth} signature should be primarily carried by the dominant Fe_{HR} phase, which is pyrite (Fig. 5). However, whereas all S5 data and most S7 data show a moderately correlated inverse trend of decreasing $\delta^{56}Fe_{auth}$ with increasing Fe_{auth}, the five S7 data from 141.5 to 137.5 cm (indicated by light blue symbols) depart from this trend toward higher $\delta^{56}Fe_{auth}$ (positive arrow in Fig. 7). The positive $\delta^{56}Fe$ vs Fe_{auth} trend of these S7 samples could reflect either a rise in $\delta^{56}Fe$ of $Fe(II)_{aq}$, or the greater presence of an isotopically enriched Fe mineral fraction. A notable feature of the S7 Fe speciation mineral profile in Fig. 5 is the correlated rise in both pyrite and Fe (oxyhydr)oxides at 141.5 to 137.5 cm, but as noted in section 3.4, there is a proportionally greater rise in latter. This suggests that a viable explanation for the distinct chemical signature of these samples would involve an enhanced input of sediment that was particularly enriched in detrital Fe (oxyhydr)oxides into the EMS basin at this time (thus our calculation of the % Fe_{auth} underestimates the detrital Fe (oxyhydr)oxide component for these samples). These detrital Fe (oxyhydr)oxide minerals must have a $\delta^{56}Fe$ signature that is isotopically heavier than the isotopic composition of the benthic Fe shuttle, such that sulphidation of this detrital Fe (oxyhydr)oxide flux during diagenesis maintains a relatively heavier $\delta^{56}Fe$ signature at higher detrital Fe (oxyhydr)oxide loadings. Such processes are consistent with the marked Fe_T/Al and $\delta^{56}Fe$ rises in this late S7 interval and the correlated Fe (oxyhydr)oxide) vs pyrite relationship evident in Fig. 5b .

The two end-member modelling of detrital mineral-authigenic mineral mixing

and the benthic shuttle model assumes that the primary control of the low $\delta^{56}Fe$ values is the Fe isotopic composition of $Fe(II)_{aq}$, which is quantitatively uptaken into pyrite by reaction with dissolved sulphide. Several experimental studies have shown that kinetic fractionation may occur between Fe(II)aq and precipitating Fe sulphides (Butler et al., 2005; Guilbaud et al., 2011; Mansour and Fantle, 2019). However, the most negative kinetic $\Delta^{56}Fe_{Fe(II)aq\text{-}pyrite}$ values in these experimental studies were obtained when only 10% of FeS precursors were reacted into pyrite. Here, the pyrite constitutes a major Fe_{HR} pool, and consequently the apparent fractionation factor must be lower. Additionally, as noted in the previous paragraph the fractionation factor could reflect a mixture of 1) precipitation in the water column and 2) sulphidation of highly reactive minerals such as Fe (oxyhydr)oxides.

4.2
Tracing euxinia in the EMS sapropels
4.2.1
Fe speciation proxies in EMS sapropels and background sediments

The Fe_{HR}/Fe_T and $CorrFe_{py}/Fe_{HR}$ ratios derived from the Fe speciation measurements are plotted against sample depth in Figs. 8a and 8c (S5 profile) and 8b and 8d (S7 profile). Using criteria summarized in Poulton and Canfield (2011) for marine sediments, the Fe_{HR}/Fe_T data indicate that the pre-sapropel sediments and sapropels in both profiles plot within the anoxic field (Figs. 8a,b). Only the post sapropel sediments fall within the possibly anoxic field. This field was defined to allow consideration of the potential for rapid deposition of sediment (e.g., during turbidite deposition) to mask water column Fe_{HR} enrichments under anoxic conditions (Raiswell and Canfield, 1998), and to account for the possible transfer of unsulphidized Fe_{HR} to Fe-rich clay minerals during early diagenesis in non-sulphidic porewaters (e.g., Poulton and Raiswell, 2002; Poulton et al., 2010). Neither of these processes has occurred in the EMS samples, and hence the Fe_{HR}/Fe_T ratios for post-sapropel samples reflect a progressive return to oxic depositional conditions (Raiswell and Canfield, 1998). Overall the trends indicated by Fe speciation are consistent with the Mo_{EF}-U_{EF} systematics (Fig. 3), which point to vertical deepening of anoxia until peak values, followed by weakening during sapropel termination.

Anoxic conditions in the pre-sapropel sediments are compatible with modeling studies on sapropel S1showing that sapropel formation is preceded by the formation of anoxic deep waters (Grimm et al., 2015; Grant et al., 2016). The Fe speciation data (Fig. 5) and $CorrFe_{py}/Fe_{HR}$ partitioning (Fig. 8) show that ~50% of Fe_{HR} in the pre-sapropel sediment is composed of pyrite, and that pyrite is approximately 20-30% of Fe_T. Nevertheless, the pre-sapropel sediments do not show any evident shift to light isotopic values (Fig. 4). Such a lack of a shift from marine sedimentary δ^{56}Fe values has been proposed to be a diagnostic feature of diagenetic pyrite formation, with anoxic, non-sulphidic conditions developing in the absence of a benthic Fe shuttle in the overlying water column (Matthews et al., 2017). Alternatively, the lack of an evident isotopic shift could occur when a large amount of highly reactive Fe gets sulphidized into pyrite (as evident for pre-sapropel sediments in Fig 5), thus muting the expression of the Fe isotope fractionation.

It is also notable that the pre-sapropel S5 sediments have slightly higher Fe_{HR}/Fe_T values than for S7, with a decrease from elevated values of ~0.5 at 126-131 cm toward values of 0.4 at the sapropel boundary. These slightly elevated Fe_{HR}/Fe_T values broadly match higher RSTE (Mn, U, V, but not Mo) and possibly higher Fe_T/Al observed in this depth range (Fig. 2), suggesting stronger anoxic, but non-sulphidic water column conditions. In this respect the 'higher than marine' δ^{56}Fe values of the pre-sapropel sediment at 116.5 to 126.5 cm (Fig. 4) are puzzling, since elevated δ^{56}Fe values (relative to marine values) are generally associated with oxidation. One possibility is that prior to the sapropel isotopically heavy Fe oxides were precipitated from Fe(II) mobilized in an oxygen minimum zone (Scholz et al., 2014).

Fe_{HR}/Fe_T and $CorrFe_{py}/Fe_{HR}$ rise at the sapropel lower boundary (Fig 8). The patterns generally follow the trends shown by Fe_T/Al, RSTE plots, Mo/U and Fe isotope depletions (Figs. 2, 3 and 4). Fe_{HR} values at the sapropel peaks constitute 80% of the total iron in the samples. Most notable is the fact that whereas both S5 and S7 show significant $CorrFe_{py}/Fe_{HR}$ enrichment (Fig. 8), apart from a few samples that plot in the 'possibly euxinic' field of Poulton and Canfield (2011), most peak sapropel samples fall in the uppermost parts of the ferruginous field or borderline 'possibly euxinic' values. No samples plot in the euxinic field *sensu stricto* ($Fe_{py}/Fe_{HR} > 0.8$).

4.2.2

Evidence for euxinia from Fe speciation vs [Mo] plots

The ferruginous field $CorrFe_{py}/Fe_{HR}$ ratios are not consistent with the Fe isotope shuttle model for euxinic basins or the behavior of RSTE such as Mo. Although both ferruginous and euxinic shuttling could lead to the formation of isotopically light authigenic Fe minerals, the conspicuous dominance of pyrite in the sapropels S5 and S7, coupled with Mo enrichments that indicate sulphidic water column conditions (Erickson and Helz, 2000; Helz et al., 2011; Hardisty et al., 2018; Helz and Vorlicek, 2019), suggests that the $CorrFe_{py}/Fe_{HR}$ ratios are likely giving an false ferruginous signal in the case of EMS sapropels 5 and 7. This is supported by Mo isotope data of sapropel S5 from the same core ($\delta^{98/95}Mo$ >2‰), which suggests that Mo uptake occurred under strongly euxinic conditions (Andersen et al., 2018).

At $[H_2S]$ > 11μM, dissolved molybdate species quantitatively convert to thiomolybdate species (Erickson and Helz, 2000), which become available for particulate uptake by minerals such as pyrite and/or is precipitated with Fe as colloidal $FeMoS_4$ (Helz et al, 2011; Vorlicek et al., 2019; section 4.3.1 below). The relationship between [Mo] and Fe speciation proxies was studied by Scott and Lyons (2012) with the aim of distinguishing between environments in which sulphide forms in porewater and euxinic sediments where sulphide is present in the water column. Fig. 9a is a modification of their Mo ppm vs DOP (degree of pyritization) plot in which Mo is plotted against $CorrFe_{py}/Fe_{HR}$. The [Mo] uptake fields defined by Scott and Lyons are transposed onto the [Mo] – $CorrFe_{py}/Fe_{HR}$ diagram, but with the 'possibly euxinic' boundary extended from Fe_{py}/Fe_{HR} = 0.7 down to 0.6. We define the lower boundary at 0.6 based on the lower limit of the average $CorrFe_{py}/Fe_{HR}$ value (0.67 ± 0.07: 1SD; Fig 9b) through the sapropel maxima. The high Fe_T/Al samples at the peak S7 conditions discussed in section 4.1 fall within this range, and as previously suggested likely represent the extreme case of a very high detrital crystalline Fe (oxyhydr)oxide flux to the EMS basin.

Our data thus suggest that there are conditions whereby Fe_{py}/Fe_{HR} ratios as low as 0.6 can occur under euxinic water column conditions. The Fe_{py}/Fe_{HR} threshold for identifying euxinia was originally placed at 0.8, based solely on observations from the Black Sea (Anderson and Raiswell, 2004). However, based on Fe speciation and trace metal data from Cretaceous Oceanic Anoxic Event 3 at Demerara Rise (März et

al., 2008), this boundary was refined to 0.7 by Poulton and Canfield (2011). The EMS sapropels S5 and S7 are characterized by a very high input of crystalline detrital Fe (oxyhydr)oxide minerals from the River Nile (Poulton and Raiswell, 2002). Central to the full sulphidation of Fe_{HR} under euxinic water column conditions is the reactivity of this Fe pool towards dissolved sulphide (which is particularly low for crystalline Fe (oxyhydr)oxides such as hematite and goethite), in addition to sulphide concentration and exposure time (Poulton et al., 2004). Given these considerations, the EMS sediments likely represent an extreme case study of recent euxinic settings, whereby the extent of pyritization of the Fe_{HR} pool is particularly limited. Nevertheless, this does suggest that the 'possibly euxinic' boundary should be refined to a lower value of 0.6. Indeed, we note that a lower limit of 0.6 better satisfies Fe_{py}/Fe_{HR} signatures in euxinic sediments deposited during Cretaceous Oceanic Event 2 at Tarfaya, Morocco (Poulton et al., 2015), which is a shallow shelf basin that likely received a high detrital sediment influx of Fe (oxyhydr)oxides. Furthermore, many past episodes of euxinia were characterized by much lower oceanic sulphate concentrations than the present day or the recent past (see Xiong et al., 2019), which would enhance the potential for more limited sulphidation of the Fe_{HR} pool, due to an overall decrease in exposure time to dissolved sulphide. Nevertheless, we stress that additional evidence, for example from trace metal systematics, is required to robustly identify the redox setting of samples that fall within this refined 'possibly euxinic' zone.

4.3

Implications for euxinic sapropel-forming conditions

4.3.1

Controls of euxinic water column formation.

The model for Mo uptake into organic-carbon rich sediments developed by Helz and Vorlicek (2019) includes a number of aspects relevant to sapropel euxinia. The model proposes that microbial sulphate reduction in the water column produces sulphide and reduces pH, thus initiating the precipitation of $FeMo(VI)S_4$ and its subsequent irreversible aging to $FeMo(IV)S_2(S_2)$. The sulphate to sulphide reduction progress increases with water depth, and is an inverse function of water column overturn rate, but positively depends on organic productivity. We first turn to the question of water column overturn rate. According to Helz and Vorlicek (2019), $FeMoS_4$ precipitation in the Black Sea occurs under high dissolved sulphide accumulation that reflects long water residence times (τ), in which dissolved [Mo]

reaches solubility equilibrium with the $FeMoS_4$ precipitate. Very low water overturn dynamics are common to both the Black Sea and peak EMS sapropel S5 ($\tau = 830^{+690}/_{-500}$ yr and $1030^{+920}/_{-520}$ yr, respectively) compared to modern oceanic overturn rates of ~100 yr (Andersen et al., 2018). The parallel slopes of the benthic shuttle plots (Fig. 6) also suggest comparable euxinic conditions in the Black Sea and EMS during S5 and S7.

This situation, however, differs in the early stages of sapropel formation. The early stages of sapropel development (S5 samples 102.5-94.5 cm; S7 samples 153.5-147 cm) are manifested by moderate Fe_T/Al increases and Fe isotope decreases, weak to moderate RSTE enrichments (Figs 2, 4 and 6) and lower than seawater $\delta^{98/95}Mo$ (Andersen et al., 2018). Nevertheless, $CorrFe_{py}/Fe_{HR}$ values for these early sapropels mostly plot above 0.6 within the euxinic field (Fig 9b: Supplement 3). Low $\delta^{98/95}Mo$ values (<-0.7‰ at peak reducing conditions) indicative of partial molybdenum uptake and a 'weak' benthic shuttle (evidenced by the much shallower Fe_T/Al –$\delta^{56}Fe$ slope in Fig 6) are shown by sapropel S1 at ODP 967 (Azrieli-Tal et al., 2014). Helz and Vorlicek (2019) suggest that these attributes could reflect intermediate degree of sulphate to sulphide reaction progress, in which isotopically depleted $FeMoS_4$ ~~to~~ forms from negatively fractionated thiomolybdate species in equilibrium with seawater MoO_4^{2-} (Kerl et al, 2017). Calculations of deep water renewal rates for S5 based on the water column U depletion indicate an approximately three-fold decline in thermal overturning circulation in the early sapropel stages (96.5 cm; $\tau = 340^{+385}/_{-325}$ yr (Andersen et al 2018). It therefore appears that water overturn (renewal) is an important factor in determining the dynamics of euxinic water column development and its manifestation in the slopes of the benthic shuttle Fe_T/Al vs $\delta^{56}Fe$ plots.

As noted in the paragraph above, in addition to longer water residence times, high organic productivity leads to an increase in the Particulate Organic Carbon Flux and sulphate to sulphide reduction progress. High export organic productivity in the Levantine basin during S5 has been demonstrated using Ba, TOC, and carbonate contents by Weldeab et al (2003), who also demonstrated that this increased productivity reflected high riverine nutrient supply. High Ba/Al ratios found in sapropels S5 and S7 in this study are compatible with Weldeab et al (2003). Thus it can be argued that both water column overturn slowdown and increased export organic productivity drive the developement of euxinic waters during S5 and S7.

4.3.2

Implications for diagenetic iron mobilization.

The proxies studied in this work demonstrate that the combined effects of the benthic Fe shuttle and the euxinic water column formation exert the primary control of Fe sulphide formation in sapropel S5 and S7. The euxinic conditions reflect the positive balance between dissolved sulphide formation and rates of reductive dissolution of descending Fe (oxyhydr)oxide minerals. Nevertheless, the potential role of diagenetic sulphidation at high Fe (oxyhydr)oxide fluxes has been recognized at peak S7 (Section 4.1.2), and may contribute in part to Fe sulphide formation throughout sapropel formation. This raises the question of the relation between the water column models proposed here and the diagenetic models of Fe-S mobilization proposedby Passier et al., 1996, Passier et al., 1997; Passier et al., 1999b). Of the two end member models, the 'low Fe model' described by Passier et al. 1996 and Passier et al., 1999b defines the scenario most compatible with our data. In this scenario, excess sulphide production within the sapropel leads to its migration into the overlying water column and underlying sediment. Such migration into the water column introduces additional dissolved sulphide (additional to that generated in the water column) for Fe-sulphide formation by reaction with descending Fe_{HR} minerals. Correspondingly, downward diffusion of sulphide into the underlying sediment could sulphidize Fe(oxyhydr)oxides below the sapropel leading to pyrite enrichment as described by Passier et al. (1996). Such a model would be compatible with the relatively high pyrite content and anoxicity of the pre-sapropel sediment, evident in both sapropel sequences (Fig. 5, Fig. 8). Nevertheless, it remains possible that pyrite in the underlying sediment formed in the anoxic water conditions preceding the sapropel formation.

Sulphidation of Fe (oxyhydr)oxides concurrent with water column pyrite formation may take place within the sapropels, as suggested in section 4.1.2 for peak S7. The critical factor with the diagenetic model described by Passier and co-workers, as with water column reactive processes described earlier (sections 4.1 and 4.2), is the rate of sulphide formation relative to Fe (oxyhydr)oxide dissolution. It is therefore clear that the syn-sapropel diagenetic Fe mobilization models of Passier and coworkers are compatible with the water body models developed in this study. Nonetheless, the powerful proxy signals for water column sulphide generation and isotopic light Fe shuttling in this study provide strong evidence for the domination of

water column Fe-S processes during the formation of sapropels S5 and S7. The redefined euxinic/ferruginous speciation Fe_{py}/Fe_{HR} = 0.6 boundary in particular reflects sedimentary preservation of a high flux of crystalline Fe (oxyhydr)oxide minerals to the Levantine basin, which resulted in a relatively low degree of sulphidation, despite the presence of euxinic bottom waters.

5. Conclusions and paleoclimate implications.

The paper presents convincing evidence from the benthic shuttle inverse Fe_T/Al vs $\delta^{56}Fe$ correlations, Mo_{EF} vs U_{EF} plots, and high [Mo] values for the development of euxinic water column conditions during sapropels S5 and S7. The data complement seawater $\delta^{98/95}Mo$ values determined for S5 by Andersen et al. (2018). In terms of these parameters, euxinic conditions in deep water sapropels S5 and S7 are comparable to those of the Black Sea.

Pyrite is the dominant authigenic mineral in both sapropels. Nevertheless, the Fe speciation data also show that Fe (oxyhydr)oxides are a significant mineral component (comprising up to 25% of total Fe in the sapropels) despite their thermodynamic instability in pyrite-forming sulphidic waters. Such Fe (oxyhydr)oxides are part of the Fe_{HR} fraction of the sapropels and thus depress Fe_{py}/Fe_{HR} ratios by their presence as unsulphidized Fe_{HR} minerals. Consequently, despite clear evidence for euxinic water column conditions and sulphidation, Fe_{py}/Fe_{HR} ratios are relatively low in these two EMS sapropels, and a decrease in the lower limit of the 'possibly euxinic' zone, from 0.7 to 0.6, is more appropriate for identifying water column euxinia. While this lower limit may be particularly specific to EMS sapropels, where detrital Fe mineral inputs from the Nile are unusually high, it may also be an appropriate boundary for identifying some more ancient episodes of ocean euxinia, where overall exposure time to dissolved sulphide may have been relatively low due to lower oceanic sulphate concentrations than at present. However, in these cases, robust additional evidence from trace metal systematics or from consideration of the mineralogy of primary Fe inputs is required to identify euxinic water column conditions.

Euxinic water column dynamics in EMS sapropels, as defined in this study in core ODP 967, are a function of two major kinetic controls. One is the extent of

sulphide production via bacterial sulphate reduction, as recently modelled by Helz and Vorlicek (2019), which explains Fe and Mo chemical and isotope systematics in both the early and peak stages of sapropels S5 and S7. The second kinetic parameter is the rate of reductive dissolution of the Fe (oxyhydr)oxide minerals that are present, which influences the location of the euxinic boundary in Fe speciation studies as well as the amount of Fe(II)aq. The interplay between these two parameters could potentially control the strength of euxinic and/or ferruginous conditions by regulating the relative supply of sulphide and ferrous ions in an anoxic basin. Water renewal times (thermohaline water overturn slowdown) and export productivity and high productivity drive the development of these strongly euxinic condition in the sapropels.

Although not a main aim of this study, a number of conclusions regarding the paleoceanographic outcomes of the Fe data can be mentioned. Sapropel S5 developed during a peak interglacial (MIS5e) that followed a strong glacial termination (MIS6), whereas S7 formation (MIS7a) was not preceded by a significant deglaciation event, but its cessation was immediately followed by MIS6 (Fig 1). Despite these different climatic boundary conditions, the redox conditions evident from RSTE, Mo_{EF}/U_{EF} values, Fe isotope depletions and Fe speciation are similar in magnitude and in the gradual evolution from weaker to more strongly developed sapropels under similar euxinic conditions. Such development is consistent with published benthic foraminiferal evidence for progressive evolution toward oxygen-depleted bottom waters prior to and during sapropels S5 and S7 (Melki et al., 2010).

Both sapropels are preceded by anoxic deep water column conditions. This conforms with the oceanic-hydrological model of Grimm et al. (2015) as noted in the introduction. This anoxia is particularly marked for S5, which is preceded by a period of elevated RSTE, elevated Fe_{HR}/Fe_T and anomalously high $\delta^{56}Fe$ values at 131-115 cm. The age interval of these samples (132 -136 ka; Fig. 2) overlaps with cold Heinrich stadial 11 (H11), for which a muted non-monsoonal freshwater signal has been identified in the EMS at ODP site 967 (Rodriques-Sanz et al, 2017). Nonetheless, despite the apparent pre-sapropel anoxic signal, the view proposed here is that the dominant factor in the formation and water column chemistry of sapropels S5 and S7 was the progressively declining thermohaline water overturning circulation.

Finally, we note the clear evidence in elevated Fe_T/Al, U/Al and Mo/Al values at 140.5-137.5 in sapropel S7 for increased freshwater input into the EMS. Since the major source of metals to the EMS Levantine basin was the River Nile (Wu et al., 2019), the implication is that increased Monsoon activity toward the termination of S7 resulted in increased weathering in the basaltic source area of the Blue Nile. The peak was followed by a gradual decline from sulphidic to anoxic non-sulphidic water conditions in S7 that possibly reflect the incoming glacial conditions.

Acknowledgements.
This research was supported by Israel Science Foundation Grant No 1140/12. SWP acknowledges support from a Royal Society Wolfson Research Merit Award and a Leverhulme Research Fellowship. The manuscript was substantially improved by the critical review comments and advice of Dr Hilde Passier, two unknown reviewers and the Editor Dr Michael Boettcher.

References

Algeo, T.J. and Tribovillard, N. (2009). Environmental analysis of paleoceanographic systems based on molybdenum-uranium covariation. *Chem. Geol*. 268, 211-225

Almogi-Labin, A., Bar-Matthews, M., Shriki, D., Kolosovsky, E., Paterne, M., Schilman, B., Ayalon, A., Aizenshtat, Z., Matthews, A. (2009). Climate variability during the last ~ 90 kyr in the southern and northern Levantine Basin as evident from the marine and speleothem records. *Quatern Sci. Rev*. 28, 2882-2896.

Andersen, M.B. Romaniello, S., Vance, D., Little, S.H., Herdman, R., Lyons, T.W., (2014). A modern framework for the interpretation of 238U/235U in studies of ancient ocean redox. *Earth Planet. Sci. Lett*., 400, 184-194.

Andersen, M.B., Matthews, A., Vance, D., Bar-Matthews, M., Archer, C., de Souza, G.F. (2018). A 10-fold decline in the deep Eastern Mediterranean thermohaline overturning circulation during the last interglacial period. *Earth Planet. Sci. Lett*. 503, 58-67.

Anderson, T. F. and Raiswell, R. (2004). Sources and mechanisms for the enrichment of highly reactive iron in euxinic Black Sea sediments: *Am. J. Science*, 304, 203–233.

Arnold G. L., Anbar, A.D., Barling, J., Lyons, T. (2004). Molybdenum isotope evidence for widespread anoxia in Mid-Proterozoic oceans. *Science* 304, 87-90.

Azrieli-Tal, I, Matthews, A., Bar-Matthews, M. Almogi -Labin, A., Vance, D., Archer, C., Teutsch, N. (2014). Evidence from molybdenum and iron isotopes and molybdenum –uranium covariation for sulphidic bottom waters during Eastern Mediterranean Sapropel S1 formation. *Earth Planet. Sci. Lett*. 393, 231-242.

Bar-Matthews, M. (2014). History of water in the Middle East and North Africa. In Holland H.D. and Turekian, K.K (eds.) Treatise on Geochemistry, Second Edition, Vol 14, pp. 109-128, Oxford: Elsevier.

Bar-Matthews, M., Ayalon, A., Gilmour, M., Matthews, A., Hawkesworth, C.J. (2003). Sea-land oxygen isotopic relationships from planktonic foraminifera and speleothems in the eastern Mediterranean region and their implication for

paleorainfall during interglacial intervals. *Geochim. Cosmochim. Acta* 67, 3181-3199.

Beard, B.L., Johnson, C.M., Skulan, J.L., Nealson, K.H., Cox, L., Sun, H. (2003a). Application of Fe isotopes to tracing the geochemical and biological cycling of Fe. *Chem. Geol.* 195, 87-117.

Beard, B.J., Johnson, C.M., Von Damm, K., Poulson, R.L. (2003b). Iron isotope constraints on Fe cycling and mass balance in oxygenated Earth oceans. *Geology* 31, 629-632.

Berger, A. and Loutre, M-F. (1999). Parameters of the Earth's orbit for the last 5 million years in 1 kyr resolution. PANGAEA, https://doi.org/10.1594/PANGAEA. Supplement to: Berger, A., Loutre, M-F. (1991). Insolation values for the climate of the last 10 million of years. *Quatern. Sci. Rev*. 10, 297-317.

Box M.R., Krom, M.D., Cliff, R.A., Bar-Matthews, M., Almogi-Labin A., Ayalon , A., Paterne, M. (2011). Response of the Nile and its catchment to millennial-scale climatic change since the LGM from Sr isotopes and major elements of East Mediterranean sediments. *Quatern. Sci. Rev*. 30, 431-442.

Brumsack, H.-J. (2006). The trace metal content of recent organic carbon-rich sediments: Implications for Cretaceous black shale formation, *Palaeogeogr. Palaeoclimatol. Palaeoecol.* 232, 344-361.

Butler, I.B., Archer, C., Vance, D., Olroyd, A., Rickard, D.T. (2005). Fe isotope fractionation on FeS formation in ambient aqueous solution. *Earth Planet Sci. Lett.* 236, 430-442

Calvert, S. E., Nielsen, B., Fontugne, M. R. (1992). Evidence from nitrogen isotope ratios for enhanced productivity during formation of eastern Mediterranean sapropels. *Nature* 359, 223-225.

Cane, T., Rohling, E.J., Kemp, A.E.S., Cooke, S., Pearce, R.B. (2002). High-resolution stratigraphic framework for Mediterranean sapropel S5: defining temporal relationships between records of Eemian climate variability. *Palaeogeogr. Palaeoclimatol. Palaeoecol.* 183, 87–101.

Canfield, D.E., Raiswell, R., Westrich, J.T., Berner, R.A. (1986). The use of chromium reduction in the analysis of reduced inorganic sulfur in sediments and shales. *Chem. Geol.* 54, 149-155.

Canfield, D.E., Raiswell., R., Bottrell, S.H. (1992). The reactivity of sedimentary iron minerals toward sulphide. *Am. J. Sci*. 292, 659-683.

Canfield, D.E., Lyons, T.W., Raiswell, R. (1996). A model for iron deposition to euxinic Black Sea sediments. *Am. J. Sci*. 296, 818-834.

Canfield, D.E., Poulton, S.W., Knoll, A.H., Narbonne, G.M., Ross, G., Goldberg, T., Strauss, H. (2008). Ferruginous conditions dominated later Neoproterozoic deep-water chemistry, *Science* 321, 949-952.

Clarkson, M.O., Poulton, S., Guilbaud, R., Wood, R. (2014). Assessing the utility of Fe/Al and Fe-speciation to record water column redox conditions in carbonate-rich sediments. *Chem. Geol.* 382, 111-122.

Craddock, P.R. and Dauphas, N. (2011). Iron isotopic compositions of geological reference materials and chrondites. *Geostandards and Geoanalytical Res.* 35, 101-123.

Dauphas, N.,John, S.G.,Rouxel, O. (2017). Iron isotope systematics. In: Teng, F-Z., Watkins, J.M., Dauphas, N. (eds) Non-traditional stable isotopes. *Rev. Mineral. Geochem.* 82, 415-510.

de Lange, G.J., Thomson, J., Reitz, A., Slomp, C.P., Speranza Principato, M., Erba, E., Corselli, C. (2008). Synchronous basin wide formation and redox-controlled preservation of a Mediterranean sapropel. *Nat. Geosci*. 1, 606–610.

Emeis, K-C., Schulze, H-M. Struck, U., Sakamoto, T., Doose, H., Erlenkeuser, H., Howell, M., Kroon, D., Paterne, M. (1998). Stable isotope and temperature records of sapropels from ODP sites 964 and 967: constraining the physical environment of sapropel formation in the Eastern Mediterranean Sea. In: Robertson A.H.F., Emeis K-C., Richter, C. and Camerlenghi, A. (eds.) *Proc. ODP Sci. Res.* 160. Ocean Drilling Program, College Station, TX, pp 309-331.

Emeis, K.C., Schulz, H., Struck, U., Rossignol-Strick, M., Erlenkeuser, H., Howell, M.W., Kroon, D., Mackensen, A., Ishizuka, S., Oba, T., Sakamoto, T., Koizumi, I. (2003). Eastern Mediterranean surface water temperatures and $\delta^{18}O$ composition during deposition of sapropels in the late Quaternary. *Paleoceanography* 18, 1005. http://dx.doi.org/10.1029/2000PA000617.

Erickson, B.E.and Helz, G.R. (2000). Molybdenum(VI) speciation in sulfidic waters: stability and lability of thiomolybdates. *Geochim. Cosmochim. Acta* 64, 1149–1158.

Escoube, R., Rouxel, O.J., Sholkovitz, E., Donard, O.F.X. (2009). Iron isotope systematics in estuaries: The case of North River, Massachusetts (USA). *Geochim. Cosmochim. Acta* 73, 4045-4059.

Fehr, M.A., Andersson, P.S., Hålenius, U., Mörth, C.-M. (2008). Iron isotope variations in Holocene sediments of the Gotland Deep. *Geochim. Cosmochim. Acta* 72, 807–826.

Fehr, M.A., Andersson, P.S, Halenius, U. Gustafsson, O., Morth, C-M. (2010). Iron enrichments and Fe isotopic compositions of surface sediments from the Gotland Deep, Baltic Sea. *Chem. Geol.* 277, 310-322.

Fillipidi, A. and de Lange, G.J. (2019). Eastern Mediterranean deep water formation during Sapropel S1: a reconstruction using geochemical records along a bathymetric transect in the Adriatic outflow region. *Paleoceanography and Paleoclimatology* 34, 409-429. https://doi.org/10.1029/2018PA003459.

Gallego-Torres, D., Martinez-Ruiz, F., de Lange, G. J., Jimenez-Espejo, F.J. Ortega-Huertas, M. (2010). Trace-elemental derived paleoceanographic and paleoclimatic conditions for Pleistocene Eastern Mediterranean sapropels. *Palaeogr, Palaeoclimat., Palaeoecol.* 293**,** 76–89**.**

Goldberg, T., Archer, C., Vance, D,. Thamdrup, B., McAnena, A., Poulton S.W. (2012), Controls on Mo isotope fractionations in a Mn-rich anoxic marine sediment, Gullmar Fjord, Sweden, *Chem.Geol*. 296,73-82**.**

Grimm, R., Maier-Reimer, E., Miklolajewicz, U., Schmiedl, G., Muller-Navarra, K., Adloff, F., Grant, K.M., Ziegler, M., Lourens, L.J., Emeis, K-C. (2015). Late glacial initiation of Holocene eastern Mediterranean sapropel formation. *Nature Commun.* 6:7099 doi: 10.1038/ncomms8099.

Grant, K.M., Rohling, E.J., Bar-Matthews, M., Ayalon, A., Medina-Elizalde, M., Ramsey, C.B., Satow, C. and Roberts, A.P. (2012). Rapid coupling between ice volume and polar temperature over the past 150,000 years. *Nature*, 491(7426), p.744.

Grant, K.M., Grimm R., Mikolajewicz, U., Marino, G., Ziegler, M., Rohling, E.J. (2016). The timing of Mediterranean sapropel deposition relative to insolation, sea-level and African monsoon changes. *Quatern. Sci. Rev.* 140,125-141.

Guilbaud, R., Butler, I.B., Ellam, R.M. (2011). Abiotic pyrite formation a large Fe isotope fractionation. *Science* 332, 1548–1551.

Hardisty, D.S., Riedinger, N, Gill, B.C., Johnston, D.T., Reinhard, C.T., Planavasky, N.J., Asael, D., Rouxel, O., Owens, J.O., Lyons, T.W. (2018). Detection of sulfidic pore fluids beneath an oxic water column: a comparison of sequential Fe and Mo paleoredox proxies at FOAM: *Am. J. Sci*. 318, 527-556.

Hennekam, R., Jilbert, T., Schnetger, B., de Lange G.J. (2014). Solar forcing of Nile discharge and sapropel S1 formation in the early to middle Holocene eastern Mediterranean, *Paleoceanography*, 29, 343–356, doi:10.1002/2013PA002553

Hennekam, R., Donders T.H., Zwiep K., de Lange, G.J. (2015). Integral view of Holocene precipitation and vegetation changes in the Nile catchment area as inferred from its delta sediments. *Quat. Sci. Rev.*130, 189-199.

Helz, G. R., Bura-Nakić, E., Mikac, N., Ciglenečki, I. (2011). New model for molybdenum behavior in euxinic waters. *Chem. Geol.* 284, 323−332.

Helz, G.R., Vorlicek, T.P (2019). Precipitation of molybdenum from euxinic waters and the role of organic matter. *Chem. Geol*. 509, 178-193.

Johnson, C.M., Beard, B L., Roden, E.E. (2008). The iron isotope fingerprints of redox and biogeochemical cycling in modern and ancient earth. *Annu. Rev. Earth Planet. Sci.* 36**,** 457–493.

Kendall, B., Dahl, T.W., Anbar, A.D. (2017). *Good Golly, Why Moly*? The stable isotope geochemistry of molybdenum. In: Teng, F-Z., Watkins, J.M., Dauphas, N. (eds) Non-traditional stable isotopes. *Rev. Mineral. Geochem.* 82, 683-732.

Kerl, C.F., Lohmayer, R., Bura-Nakic, E., Vance, D., Planer-Friedrich, B. (2017). Experimental confirmation of isotope fractionation in thiomolybdates using ion chromatographic separation and detection by Multicollector ICPMS. *Anal. Chem*. 89, 3123–3129.

Kondratev, S.I., Mendevedev, E.V., Konovalov, S.K. (2017). Total alkalinity and pH of the Black Sea waters in 2010-2011. *Physical Oceanography* doi:10.22449/1573-160X-2017-4-35-45.

Langgut, D., Almogi-Labin, A., Bar-Matthews, M., Weinstein-Evron, M. (2011). Vegetation and climate changes in the South Eastern Mediterranean during the Last Glacial-Interglacial cycle (86 ka): new marine pollen record. *Quatern. Sci. Rev.* 30, 3960-3972.

Langmuir, D. (1997) *Aqueous Environmental Geochemistry*, Prentice Hall, Upper Saddle, NJ-[PDF]researchgate.net

Lyons T.W. and Severmann S. (2006). A critical look at paleoredox proxies: new insights from modern euxinic marine basins. *Geochim. Cosmochim. Acta*. 70, 5698-5722.

Lyons, T.W., Anbar, A.D., Severmann, S., Scott C., Gill B. C. (2009). Tracking euxinia in the ancient ocean: a multiproxy perspective and Proterozoic case study. *Ann. Rev. Earth Planet. Sci.* 37: 507-534.

Mansor, M. and Fantle, M.S. (2019). A novel framework for interpreting pyrite-based Fe isotope records of the past. *Geochim. Cosmochim. Acta* 253, 39-62.

März, C, Poulton, S.W., Beckmann, B., Kuster, T., Wagner, S. Kasten, S. (2008). Redox sensitivity of P cycling during marine black shale formation: Dynamics of sulfidic and anoxic, non-sulfidic bottom waters. *Geochim. Cosmochim.Acta* 73, 3703-3717

Matthews, A., Azrieli-Tal, I., Benkovitz, A., Bar-Matthews, M., Vance, D., Poulton, S.W., Teutsch, N., Almogi-Labin, A., Archer, C. (2017). Anoxic development of sapropel S1 in the Nile Fan inferred from redox sensitive proxies, Fe speciation, Fe and Mo isotopes. *Chem. Geol*. 475, 24-39.

Meyers, P.A. (2006). Paleogeographic and paleoclimate similarities between Mediterranean sapropels and Cretaceous black shales. *Paleogeog. Paleoclimatol. Paleoecol.* 235, 305-320.

Meyer, K.L., Kump, L.R. (2008). Oceanic euxinia in earth history: causes and consequences. *Annu. Rev. Earth Planet. Sci.* 36, 251–288.

Melki, T., Kallel., N., Fontugne., M. (2010). The nature of transitions from dry to wet condition during sapropel events in the Eastern Mediterranean Sea. *Palaeogr. Palaeoclim. Palaeoecol.* 291, 267-285.

Nägler, T.F., Neubert, N., Böttcher, M.E., Dellwig O., Schnetger, B. (2011). Molybdenum isotope fractionation in pelagic euxinia: evidence from the modern Black and Baltic Seas. *Chem. Geol.* 289, 1–11.

Neubert, N., Nägler, Th.F., Böttcher, M.E. (2008). Sulfidity controls molybdenum isotope fractionation in euxinic sediments: evidence from the modern Black Sea. *Geology* 36, 775–778.

Nijenhuis, I.A., Bosch, H.-J., Sinninghe-Damste, J.S., Brumsack, H.-J., de Lange, G.J. (1999). Organic matter and trace element rich sapropels and black shales: a geochemical comparison. *Earth Planet. Sci. Lett.* 169, 277–290.

Osborne, A.H., Vance, D., Rohling, E.J., Barton, N., Rogerson, M., Fello, N. (2008).

A humid corridor across the Sahara for the migration of early modern humans out of Africa, 120,000 years ago. *Proc. Natl. Acad. Sci. USA* 105, 16444-16447.

Passier, H.F., Middelburg, J.J., van Os, B.J.H., de Lange G.J. (1996) Diagenetic pyritization under eastern Mediterranean sapropels caused by downward sulphide diffusion. *Geochim. Cosmochim. Acta* 60, 751-763.

Passier, H.F., de Lange G.J., Middelburg, J.J., Böttcher, M.E. (1997). Pyrite contents, microtextures, and sulphur isotopes in relation to formation of the youngest eastern Mediterranean sapropel. *Geology* 25, 519-522.

Passier, H.F., Bosch, H-J., Nijenhuis, I.A., Lucas, I.j., Lourens, J., Boettcher, M.E., Leenders, A., Sinninghe Damste J.S., de Lange, G.J. and de Leeuw, J.W. (1999a). Sulphidic Mediterranean surface waters during Pliocene sapropel formation. *Nature* 397, 146-149.

Passier, H.F., Middelburg, J.J. de Lange G.J., Böttcher, M.E. (1999b). Modes of sapropel formation in the eastern Mediterranean: some constraints based on pyrite properties. *Mar Geol*. 153, 199-219.

Poitrasson, F., Vieira, L.C., Seyler, P., dos Santos Pinheiro, G.M., Mulholland, D.S., Bonnet, M.-P., Martinez, J.-M., Lima, B.A., Boaventura, G.R., Chmeleff, J. (2014). Iron isotope composition of the bulk waters and sediments from the Amazon River Basin. *Chem. Geol.* 377, 1-11.

Poulton, S.W., Krom, M.D., Raiswell, R. (2004). A revised scheme for the reactivity of iron (oxyhydr)oxide minerals towards dissolved sulfide. *Geochim. Cosmochim. Acta* 68, 3703-3715.

Poulton, S.W. and Raiswell, R. (2002). The low-temperature geochemical cycle of iron: from continental fluxes to marine sediment deposition. *Am. J. Sci.* 302, 774-805.

Poulton, S.W. and Canfield, D.E. (2005). Development of a sequential extraction procedure for iron: implications for iron partitioning in continentally derived particulates. *Chem. Geol.* 214, 209-221.

Poulton S.W., Fralick, P.W., Canfield D.E. (2010). Spatial variability in oceanic redox structure 1.8 billion years ago, *Nature Geoscience* 3, 486-490.

Poulton, S.W. and Canfield, D.E. (2011). Ferruginous conditions: a dominant feature of the ocean through earth's history. *Elements* 7, 107-112.

Poulton, S.W., Henkel, S., März, C., Urquhart, C., Flögel, S., Kasten, S, Sinninghe Damste, J.S., Wagner, T. (2015). A continental-weathering control on orbitally driven redox-nutrient cycling during Cretaceous Oceanic Anoxic Event 2. *Geology* 43, 963-966.

Raiswell, R., Reinhard, C.T., Derkowski, A., Owens. J., Bottrell, S.H., Anbar, A.D., Lyons, T.W. (2011). Formation of syngenetic and early diagenetic iron minerals in the late Archean Mt. McRae Shale, Hamersley Basin, Australia: New insights on the patterns, controls and paleoenvironmental implications of authigenic mineral formation. *Geochim. Cosmochim. Acta* 75, 1072-1087.

Raiswell, R. and Canfield, D.E. (1998). Sources of iron for pyrite formation in marine sediments. *Am. J. Sci.* 298, 219-245.

Raiswell, R. and Canfield, D.E. (2012). The iron biogeochemical cycle past and present. *Geochem. Perspectives*. 1, 220 pp.

Raiswell, R., Hardisty, D.S., Lyons, T.W., Canfield, D.D., Owens, J.D., Planavsky, N.J., Poulton, S.W., Reinhard, C.T. (2018). The iron paleoredox proxies: A guide to the pitfalls, problems and proper practice. *Am. J. Sci.* 318, 491-526.

Reitz, A., Wille, M., Nägler, T.F., de Lange, G.J. (2007). Atypical Mo isotope signatures in eastern Mediterranean sediments. *Chem. Geol*. 245, 1–8.

Rodríguez-Sanz, L.**,** Bernasconi, S. M., Marino, G., Heslop, D., Müller, I. A., Fernandez, A., Grant, K. M., & Rohling, E. J., (2017). Penultimate deglacial warming across the Mediterranean Sea revealed by clumped isotopes in foraminifera. *Sci. Rep.* 7(1): 16572. doi:10.1038/s41598-017-16528-6.

Rohling, E. J. (1994). Review and new aspects concerning the formation of eastern Mediterranean sapropels. *Mar. Geol.* 122, 1-28.

Rohling, E.J., Hilgen, F.J., 1991. The eastern Mediterranean climate at times of sapropel formation: a review. *Geologie en Mijnbouw* 70, 253-264.

Rohling, E.J., Hopmans, E.C., Sinninghe-Damsté, J.S. (2006). Water column dynamics during the last interglacial anoxic event in the Mediterranean (sapropel S5). *Paleoceanography* 21, PA2018. http://dx.doi.org/10.1029/2005PA001237.

Rohling, E. J., Marino, G., Grant, K. M. (2015). Mediterranean climate and oceanography, and the periodic development of anoxic events (sapropels) (2015). *Earth-Sci. Rev*. 143, 62–97.

Revel, M., Colin, C., Bernasconi, S., Combourieu-Nebout, N.,Ducassou, E., Grousset, F., Rolland, Y., Migeon, S., Bosch, D., Brunet, P., Zhao, Y., and Mascle, J.

(2014). 21 000 years of Ethiopian African monsoon variability recorded in sediments of the western Nile deep-sea fan, *Reg. Environ. Change*, 14, 1685–1696, doi:10.1007/s10113-014-0588-x.

Rosentraub, Z. and Brenner, S. (2007). Circulation over the southeastern continental shelf and slope of the Mediterranean Sea: direct current measurements, winds, and numerical model simulations. *J. Geophys. Res*. 112, C11001. doi:10.1029/2006JC003775.

Rossignol-Strick, M., Nesteroff, V., Olive, P., Vergnaud-Grazzini, C. (1982). After the deluge: Mediterranean stagnation and sapropel formation. *Nature* 295, 105–110.

Rossignol-Strick, M. (1985). Mediterranean Quaternary sapropels: an immediate response to of the African Monsoon to variation of insolation. *Paleogeog. ,Paleoclimatol. Paleoecol.* 49, 237–265.

Rossignol-Strick, M. (1985). Mediterranean Quaternary sapropels: an immediate response to of the African Monsoon to variation of insolation. *Paleogeogr. Paleoclimatol. Paleoecol*. 49, 237-265.

Scheiderich, K, Zerkl, A.L Helz, G.R. Farquhar, J., Walker, R.J. (2010). Molybdenum isotope, multiple sulfur isotope, and redox-sensitive element behavior in early Pleistocene Mediterranean sapropels. *Chem.Geol*, 279, 134-144.

Scholz, F., Severmann, S., McManus, J., Hensen, C. (2014). Beyond the Black Sea paradigm. The sedimentary fingerprint of an open –marine iron shuttle. *Geochim. Cosmochim. Acta,* 127, 368-380.

Scott, C. and Lyons, T.W. (2012).. Contrasting molybdenum cycling and isotopic properties in euxinic versus non-euxinic sediments and sedimentary rocks: refining the paleoproxies. *Chem. Geol*. 324–325, 19–27.

Scrivner, A.E., Vance, D., Rohling, E.J. (2004). New neodymium isotope data quantify Nile involvement in Mediterranean anoxic episodes. *Geology* 32, 565–568..

Severmann, S., Lyons, T.W., Anbar, A., McManus, J., Gordon, G. (2008). Modern iron isotope perspective on Fe shuttling in the Archean and the redox evolution of ancient oceans. *Geology* 36, 487–490.

Severmann S., McManus J., Berelson W.M., Hammond, D.E. (2010). The continental shelf benthic iron flux and its isotope composition. *Geochim. Cosmochim. Acta,* 74, 3984-4004.

Stookey, L.L. (1970). Ferrozine – a new spectrophotometric reagent for iron. *Anal. Chem.* 42, 779-781.

Tachikawa, K., Vidal, L., Cornuault, M., Garcia, M., Pothin, A., Sonzogni, C., Bard, E., Menot, G, Revel, M. (2015). Eastern Mediterranean Sea circulation inferred from the conditions of S1 sapropel deposition. *Clim. Past*. 11, 855-86.

Teutsch, N., von Gunten, U., Porcelli, D., Cirpka, O.A., Halliday, A.N. (2005). Adsorption as a Cause for Iron Isotope Fractionation in Reduced Groundwater. *Geochim. Cosmochim. Acta.* 69: 4175-4185.

Teutsch, N., Schmid, M., Muller, B., Halliday, A.N., Burgmann, H., Wehrli, B. (2009). Large iron isotope fractionation at the oxic–anoxic boundary in Lake Nyos. *Earth. Planet. Sci. Lett.* 285, 52-60.

Thomson, J., Mercone, D., de Lange, G.J., van Santvoort, P.J.M. (1999). Review of recent advances in the interpretation of Eastern Mediterranean sapropel S1 from geochemical evidence. *Mar. Geol.* 153, 77–89.

Tribovillard, N., Algeo, T.J., Lyons, T., Riboulleou, T. (2006). Trace elements as paleoredox and paleoproductivity proxies: an update. *Chem Geol*. 232, 12-32.

van Helmond, N.A.G.M., Hennekam, R., Donders, T.H., Bunnik, F.P.M., de Lange, G.J., Brinkhuis, H., Sangiorgi, F. (2015). Marine productivity leads organic matter preservation in sapropel S1: palynological evidence from a core east of the Nile River outflow. *Quatern. Sci. Rev*. 108, 130-138.

van Santvoort, P.J.M., De Lange, G.J., Thomson, J., Cussen, H., Wilson, T.R.S., Krom, M.D., Strohle, K. (1996). Active post-depositional oxidation of the most recent sapropel (S1) in the eastern Mediterranean. *Geochim. Cosmochim. Acta* 60, 4007–4024.

Vance, D., Scrivner, A.E., Beney, P, Staubwasser, M, Henderson, G.F., Stowell, N.C. (2004). The use of foraminifera as a record of past neodymium isotope composition of seawater. *Paleoceanography*,19, PA2009. doi:10.1029/2003PA000957.

Vorlicek, T.P., Helz, G.R., Chappaz, A., Vue, P., Vezina, A., Hunter, W. (2018). Molybdenum burial mechanism in sulfidic sediments: iron-sulphide pathway.

ACS Earth Space Chem. 2(6) 565-575.

Warning B. and Brumsack, H-J. (2000). Trace metal signatures of eastern Mediterranean sapropels. *Paleogeogr. Paleoclimatol. Paleoecol.* 158, 293-309.

Wegwerth, A., Eckert, S., Dellwig, O., Schnetger, B., Severmann, S., Weyer, S., Brüske, A., Kaiser, J., Köster, J., Arz, H.W., Brumsack, H.J. (2018). Redox evolution during Eemian and Holocene sapropel formation in the Black Sea. *Palaeogeog. Palaeoclimatol. Palaeoecol*. 489**,** 249-260.

Weldeab, S., Emeis, K.-C., Hemleben, C., Schmiedl, G., Schulz, H. (2003). Spatial productivity variations during formation of sapropels S5 and S6 in the Mediterranean Sea: Evidence from Ba contents. *Palaeogeogr. Palaeoclim., Palaeoecol.*, 191(2), 169–190. http://doi.org/10.1016/S0031-0182(02)00711-3.

Wijsman, J.W.M., Middelburg, J.J., Heip, C.H.R. (2001). Reactive iron in Black Sea sediments: implications for iron cycling. *Marine Geol*. 172, 167–180.

Wu, J., Filippidi, A., Davies, G. R., & De Lange, G. J. (2018). Riverine supply to the eastern Mediterranean during last interglacial sapropel S5 formation: A basin-wide perspective. Chem. Geol. 485, 74–89. http://doi.org/10.1016/j.chemgeo.2018.03.037

Wu, J., Pahnke, K., Boning, P., Wu. L., Michard, A., de Lange, G.J. (2019). Divergent Mediterranean seawater circulation during Holocene sapropel formation- reconstructed using Nd isotopes in fish debris and foraminifera. *Earth Planet. Sci Lett.* 511, 141-153.

Xiong, Y., Guilbaud, R., Peacock, C.L., Cox, R.P., Canfield, D.E., Krom, M.D., Poulton, S.W. (2019). Phosphorus cycling in Lake Cadagno, Switzerland: A low sulfate euxinic ocean analogue. *Geochim. Cosmochim. Acta*, 251, 116-135.

Zegeye, A., Bonneville, S., Benning, L., Sturm, A., Fowle, D.A., Jones, C., Canfield, D.E., Ruby, C. Maclean, L.C., Nomosatryo, S., Crowe, S.A., Poulton, S.W. (2012). Green rust formation controls nutrient availability in a ferruginous water column. *Geology* 40, 599-602.

Figure Captions

Figure 1 Upper diagram: July insolation values at 65°N at 1 ky resolution (Berger and Loutre, 1999) and Probalistic Relative Sea Level (RSL) values (Grant et al., 2012) covering the estimated formation periods of sapropels S5 and S7. Lower diagram: Location of core site ODP-967 and other sites mentioned in the text in the Eastern Mediterranean Sea (EMS). White arrows indicate surface waters circulation pattern (Rosentraub and Brenner, 2007.

Figure 2 Total organic carbon (TOC) and elemental depth profiles for sapropels S5 and S7 and their enclosing non-sapropelic sediments. TOC profiles are taken from Emeis et al. (1998); elemental profiles normalized to Al are from this study (Table 1). Vertical dashed lines indicate the sapropel boundaries determined from Ba/Al and TOC trends, and the yellow area indicates the sapropel.
Fig 2A: Depth profiles covering sapropel S5. Ages in ka at the top of the diagram are as independently determined by Grant et al. (2012).
Figure 2B: Depth profiles covering sapropel S7. Ages in ka at the top of the diagram are as given by Emeis et al. (2003), based on sapropel initiation at 197 ka at peak insolation.

Figure 3 Mo_{EF} vs U_{EF} diagram showing pre-sapropel, sapropel and post-sapropel authigenic Mo and U enrichment factor variations. The red line indicates the seawater Mo_{EF}/U_{EF} trend. The green arrows show schematic evolution in enrichment factor trajectories based on physical and chemical controls on water masses estimated by Algeo and Tribovillard (2009). Data Source: Table 1.

Figure 4 Variations in Fe_T/Al (blue font) and $\delta^{56}Fe$ (red font) of sapropel and pre- and post-sapropel samples as a function of profile depth. Dashed lines and yellow areas indicate the sapropels. The range of $\delta^{56}Fe$ values for oxygenated marine sediments is indicated by the thick red vertical bar. Data source: Table 1. (a) sapropel S5 profile. (b) sapropel S7 profile.

Figure 5 Variations in wt% of highly reactive Fe (Fe_{HR}) pools as a function of depth. The F esulphide pool (predominantly pyrite) prior to post sampling oxidation is given

as $CorrFe_{py}$ values determined by adding the $Fe(III)_{HCl}$ and Fe_{py} wt% values (see text for further explanation). The Fe(II)HCl pool represents unsulphidized Fe(II). Sapropel boundaries as in Fig 4. (a) sapropel S5 profile. (b) sapropel S7 profile. Data source: Supplement 3.

Figure 6 Fe_T/Al vs. $\delta^{56}Fe$ for sapropels S5 (red data points) and S7 (blue data points). Also, shown for reference by green arrowed lines are the benthic Fe shuttle trends for the Black Sea (Severmann et al., 2008) and Holocene sapropel S1 at ODP967 (Azrieli-Tal et al., 2014), respectively, interpreted to reflect strong and weakly euxinic water conditions. Most S5 and S7 data plot along an inverse Fe_T/Al –$\delta^{56}Fe$ trend parallel to that of the Black Sea. However, a number of sapropel S7 samples at peak Fe/Al values (140.5- 137.5 cm)) clearly deviate from the main trend, exhibiting higher $\delta^{56}Fe$ values than would be anticipated by the main inverse trend.

Figure 7 Fe_T/Al vs. $\delta^{56}Fe$ for sapropels S5 (red data points) and S7 (blue data points). Also, shown for reference by green arrowed lines are the benthic Fe shuttle trends for the Black Sea (Severmann et al., 2008) and Holocene sapropel S1 at ODP967 (Azrieli-Tal et al., 2014), respectively, interpreted to reflect strong and weakly euxinic water conditions. Most S5 and S7 data plot along an inverse Fe_T/Al –$\delta^{56}Fe$ trend parallel to that of the Black Sea. However, a number of sapropel S7 samples at peak Fe/Al values (140.5- 137.5 cm)) clearly deviate from the main trend, exhibiting higher $\delta^{56}Fe$ values than would be anticipated by the main inverse trend.

Figure 8 Fe speciation plots of Fe_{HR}/Fe_T and $CorrFe_{py}/Fe_{HR}$ (after Poulton and Canfield, 2011). Sapropel S5 plots are given in Figs (a) and (c), respectively; sapropel S7 plots are given in Figs (b) and (d) respectively. In the $CorrFe_{py}/Fe_{HR}$ plots, the lower limit (0.8) of the euxinic sediments is defined by modern Black Sea data, whereas the lower limit for the possibly euxinic field is defined by Phanerozoic organic carbon-rich (OAE3) sediments (März et al., 2008). The Fe_{HR}/Fe_T plots show that pre-sapropel samples and sapropels from both S5 and S7 plot within the anoxic field, with Fe_{HR}/Fe_T values reaching 0.8 (i.e., highly reactive Fe becomes the dominant Fe component of the mineral assemblage). $CorrFe_{Py}/Fe_{HR}$ values of sapropels mainly plot within the ferruginous field or straddle the boundary with the

possibly euxinic field. The five sapropel samples from S7 at 141.5 to 137.5 cm exhibiting the deviations to heavier $\delta^{56}Fe_{auth}$ values in Figs. 6 and 7 plot within the overall trends of all peak sapropel samples.

Figure 9 Cross-plots of $CorrFe_{py}$ vs Mo (ppm) concentration [Mo] (Fig 9a) and $CorrFe_{py}$ vs Fe_{HR}/Fe_T (Fig 9b). Fields and boundaries in Fig 9a are taken from Scott and Lyons (2012) and those for Fig 9b are modified from Poulton and Canfield, 2011; Raiswell et al., 2018), with the lower limit of the 'possibly euxinic' zone reduced to $Fe_{py}/Fe_{HR} = 0.6$ (see main text for details).

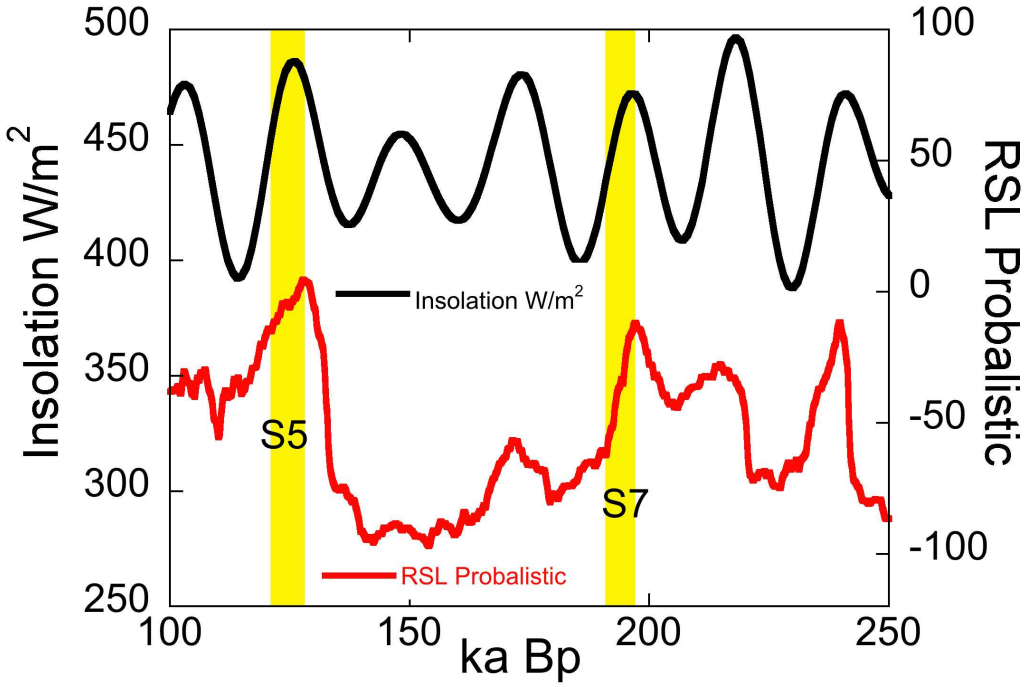
500
450
400
350
300
250
Insolation W/m2
100
50
0
-50
-100
RSL Probalistic
Insolation W/m2
RSL Probalistic
S5
S7
100
150
200
250
ka Bp

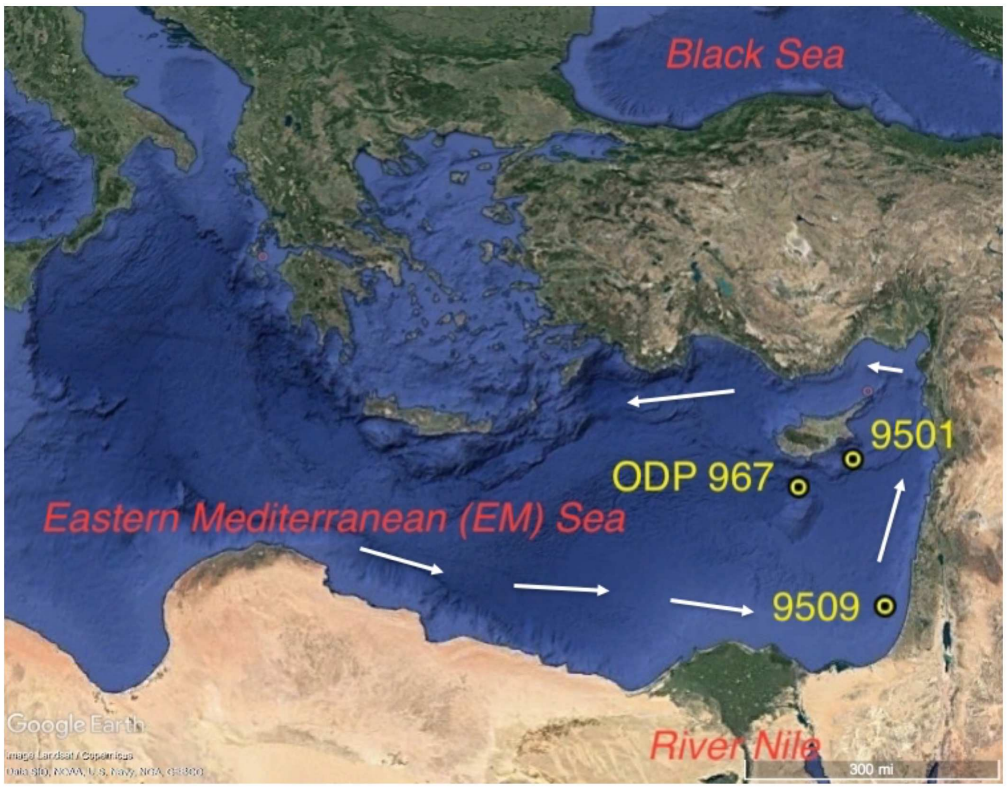
Black Sea
9501
ODP 967
Eastern Mediterranean (EM) Sea
9509
River Nile
Google Earth
300 mi

Figure 1

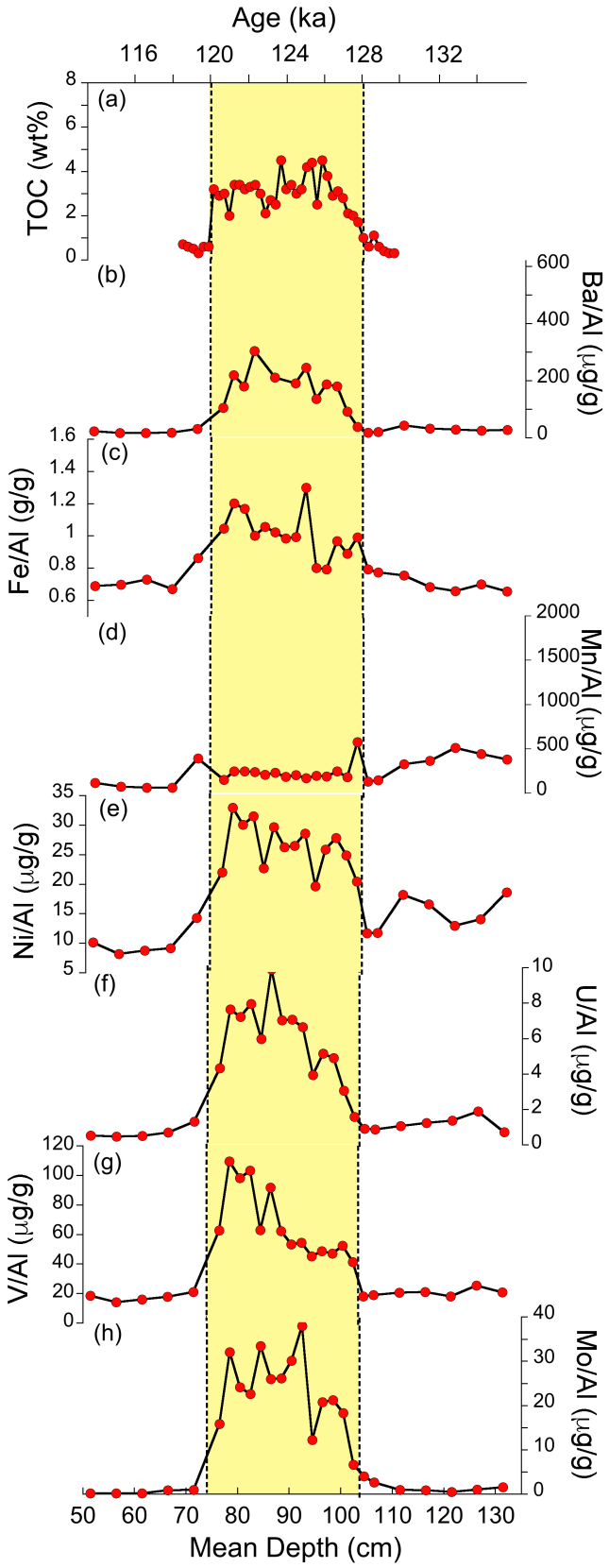
Age (ka)
116
120
124
128
132
(a)
TOC (wt%)
(b)
Ba/Al (μg/g)
(c)
Fe/Al (g/g)
(d)
Mn/Al (μg/g)
(e)
Ni/Al (μg/g)
(f)
U/Al (μg/g)
(g)
V/Al (μg/g)
(h)
Mo/Al (μg/g)
Mean Depth (cm)

FIGURE 2A

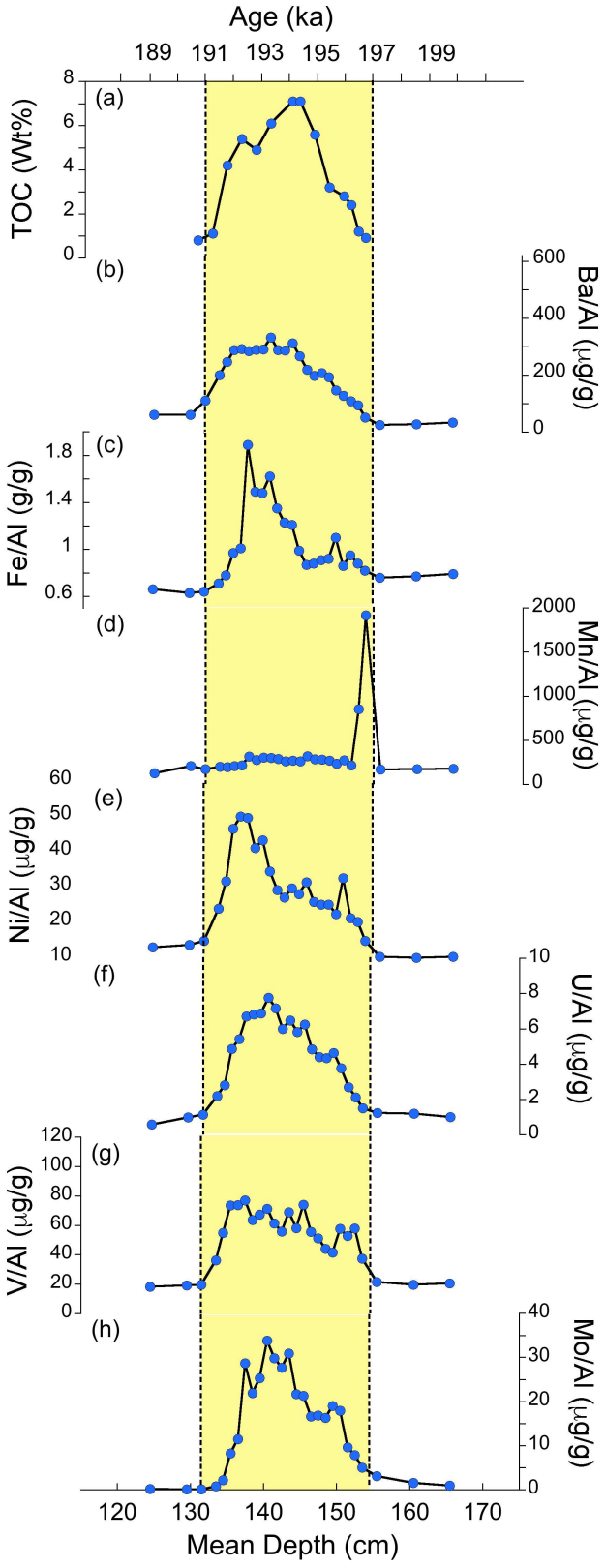
Age (ka)
189
191
193
195
197
199
(a)
TOC (Wt%)
8
6
4
2
0
(b)
Ba/Al (μg/g)
600
400
200
0
(c)
Fe/Al (g/g)
1.8
1.4
1
0.6
(d)
Mn/Al (μg/g)
2000
1500
1000
500
0
(e)
Ni/Al (μg/g)
60
50
40
30
20
10
(f)
U/Al (μg/g)
10
8
6
4
2
0
(g)
V/Al (μg/g)
120
100
80
60
40
20
0
(h)
Mo/Al (μg/g)
40
30
20
10
0
120
130
140
150
160
170
Mean Depth (cm)

Figure 2B

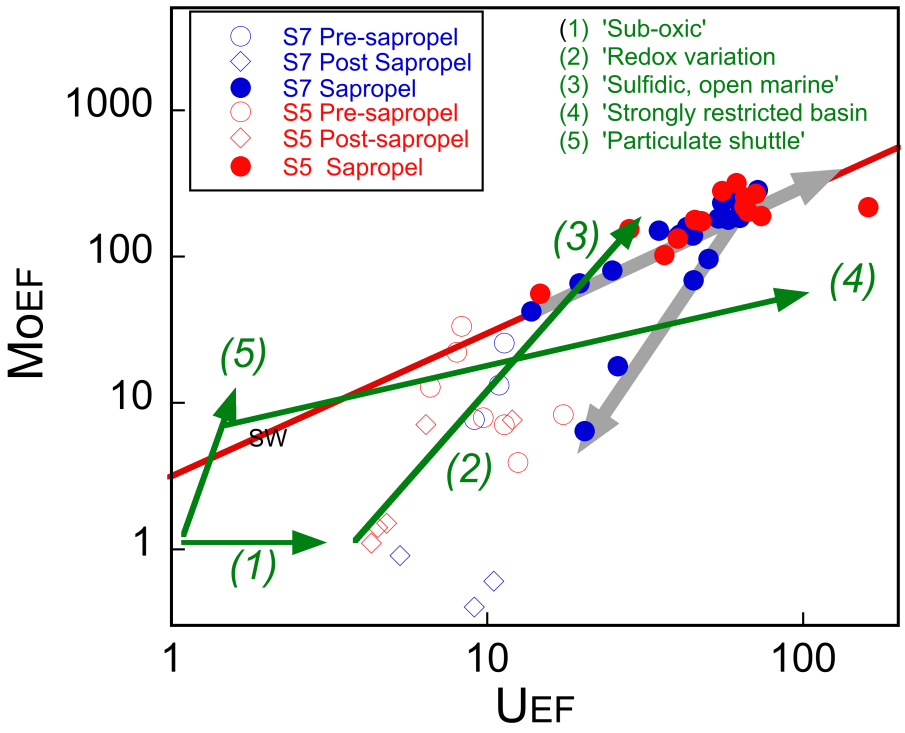
S7 Pre-sapropel
S7 Post Sapropel
S7 Sapropel
S5 Pre-sapropel
S5 Post-sapropel
S5 Sapropel
(1) 'Sub-oxic'
(2) 'Redox variation
(3) 'Sulfidic, open marine'
(4) 'Strongly restricted basin
(5) 'Particulate shuttle'
1000
100
10
1
MoEF
1
10
100
UEF
(1)
(2)
(3)
(4)
(5)
SW

Figure 3

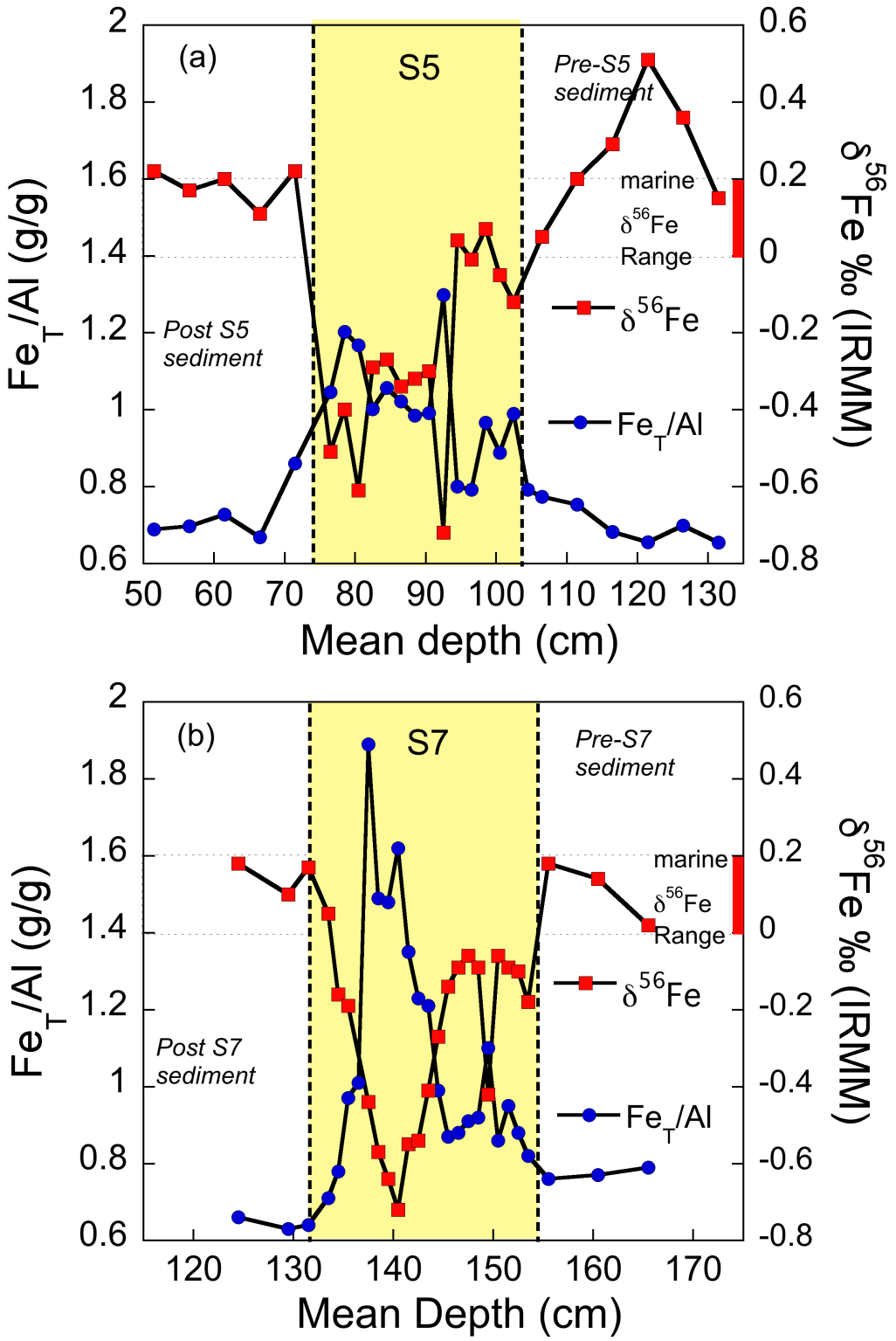
(a)
S5
Pre-S5 sediment
Post S5 sediment
marine δ56Fe Range
δ56Fe
FeT/Al
FeT/Al (g/g)
δ56Fe ‰ (IRMM)
Mean depth (cm)
(b)
S7
Pre-S7 sediment
Post S7 sediment
marine δ56Fe Range
δ56Fe
FeT/Al
FeT/Al (g/g)
δ56Fe ‰ (IRMM)
Mean Depth (cm)

Figure 4

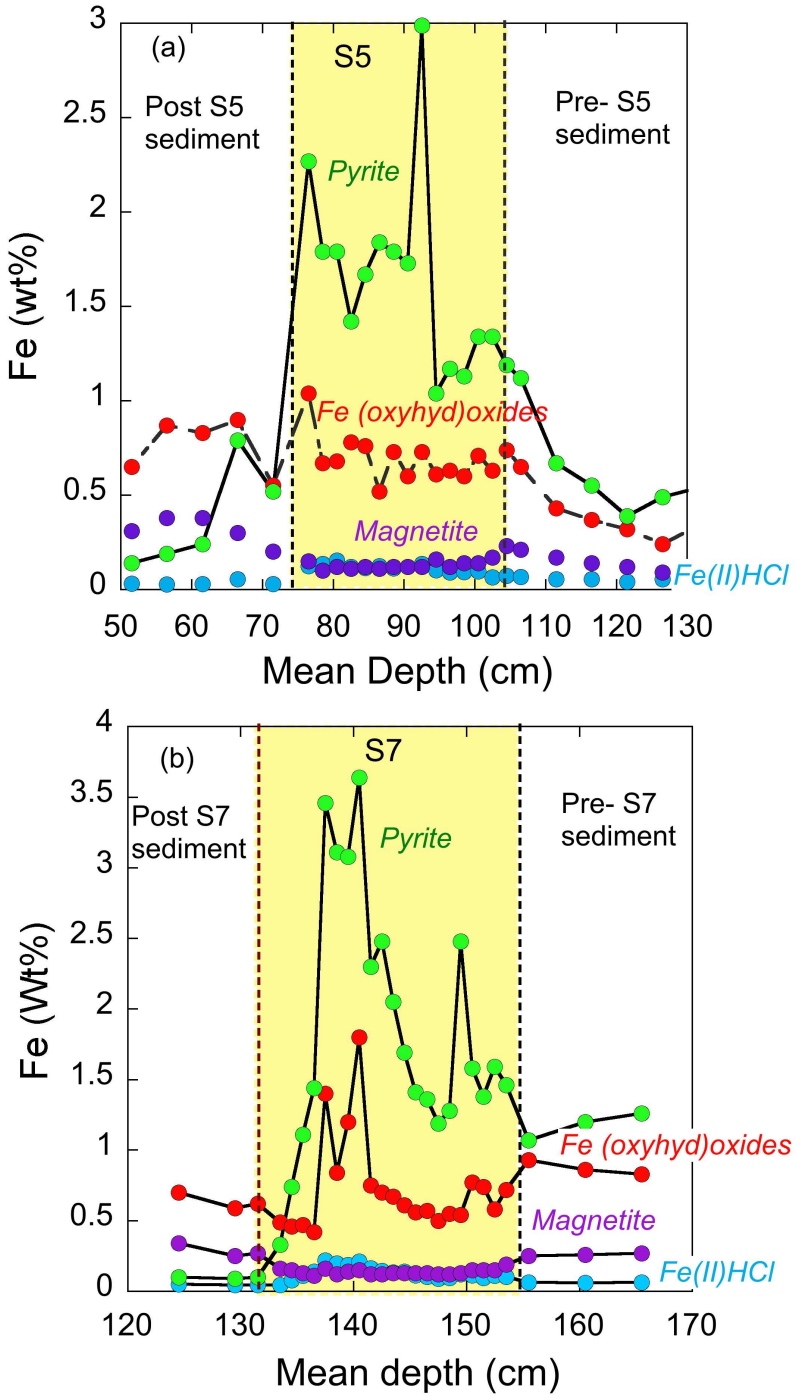
(a)
S5
Post S5 sediment
Pre- S5 sediment
Pyrite
Fe (oxyhyd)oxides
Magnetite
Fe(II)HCl
Fe (wt%)
Mean Depth (cm)
(b)
S7
Post S7 sediment
Pre- S7 sediment
Pyrite
Fe (oxyhyd)oxides
Magnetite
Fe(II)HCl
Fe (Wt%)
Mean depth (cm)

Figure 5

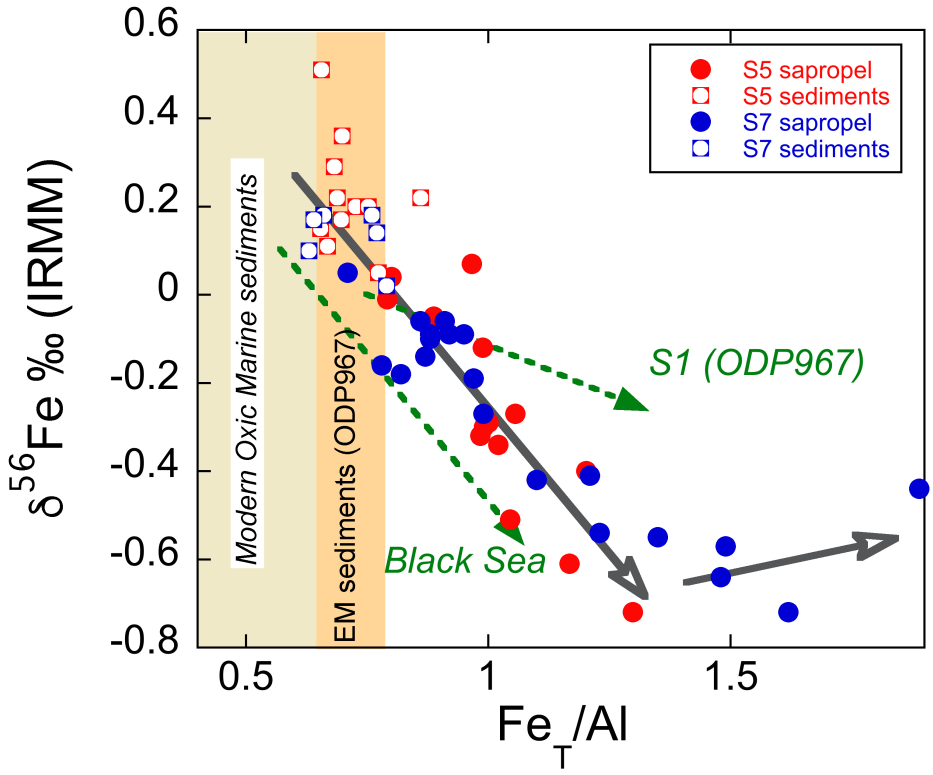
0.6
0.4
0.2
0
-0.2
-0.4
-0.6
-0.8
0.5
1
1.5
δ56Fe ‰ (IRMM)
FeT/Al
Modern Oxic Marine sediments
EM sediments (ODP967)
S5 sapropel
S5 sediments
S7 sapropel
S7 sediments
S1 (ODP967)
Black Sea

Figure 6

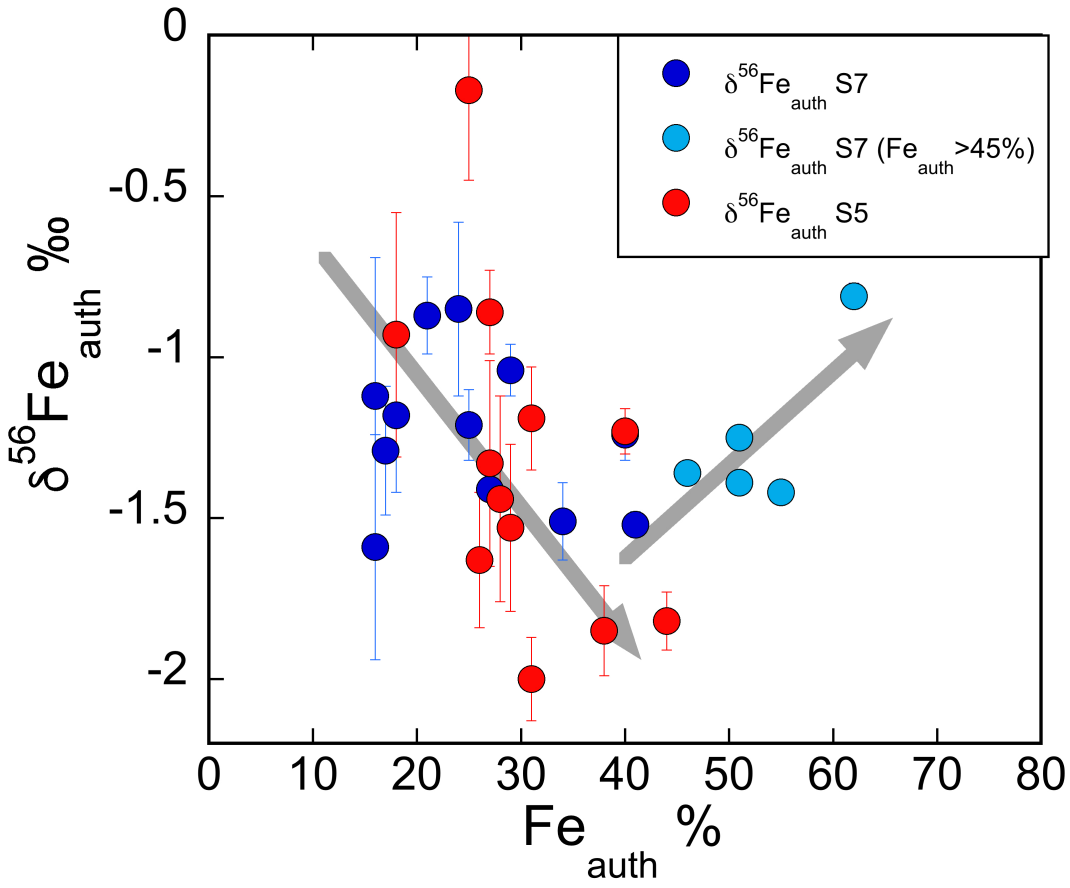
0
-0.5
-1
-1.5
-2
δ56Feauth ‰
0
10
20
30
40
50
60
70
80
Feauth %
δ56Feauth S7
δ56Feauth S7 (Feauth >45%)
δ56Feauth S5

Figure 7

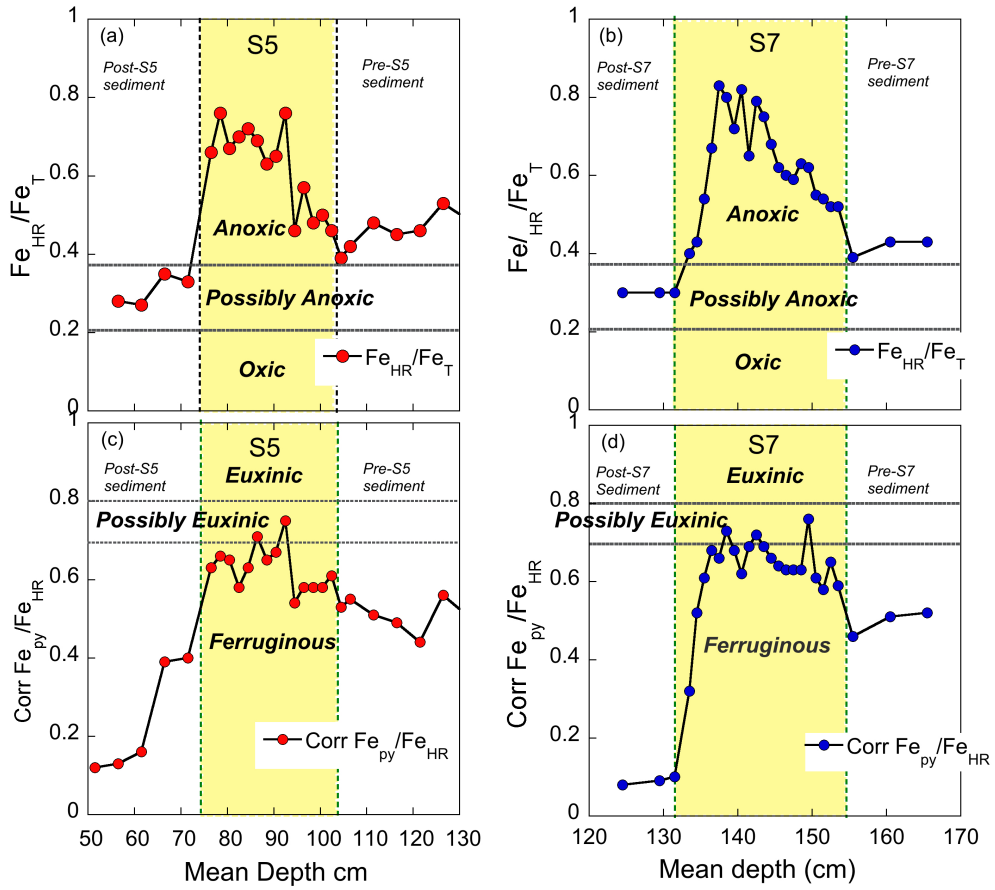
(a)
S5
Post-S5 sediment
Pre-S5 sediment
Anoxic
Possibly Anoxic
Oxic
Fe_HR/Fe_T
(b)
S7
Post-S7 sediment
Pre-S7 sediment
Anoxic
Possibly Anoxic
Oxic
Fe_HR/Fe_T
(c)
S5
Euxinic
Post-S5 sediment
Pre-S5 sediment
Possibly Euxinic
Ferruginous
Corr Fe_py/Fe_HR
Mean Depth cm
(d)
S7
Euxinic
Post-S7 Sediment
Pre-S7 sediment
Possibly Euxinic
Ferruginous
Corr Fe_py/Fe_HR
Mean depth (cm)

Figure 8

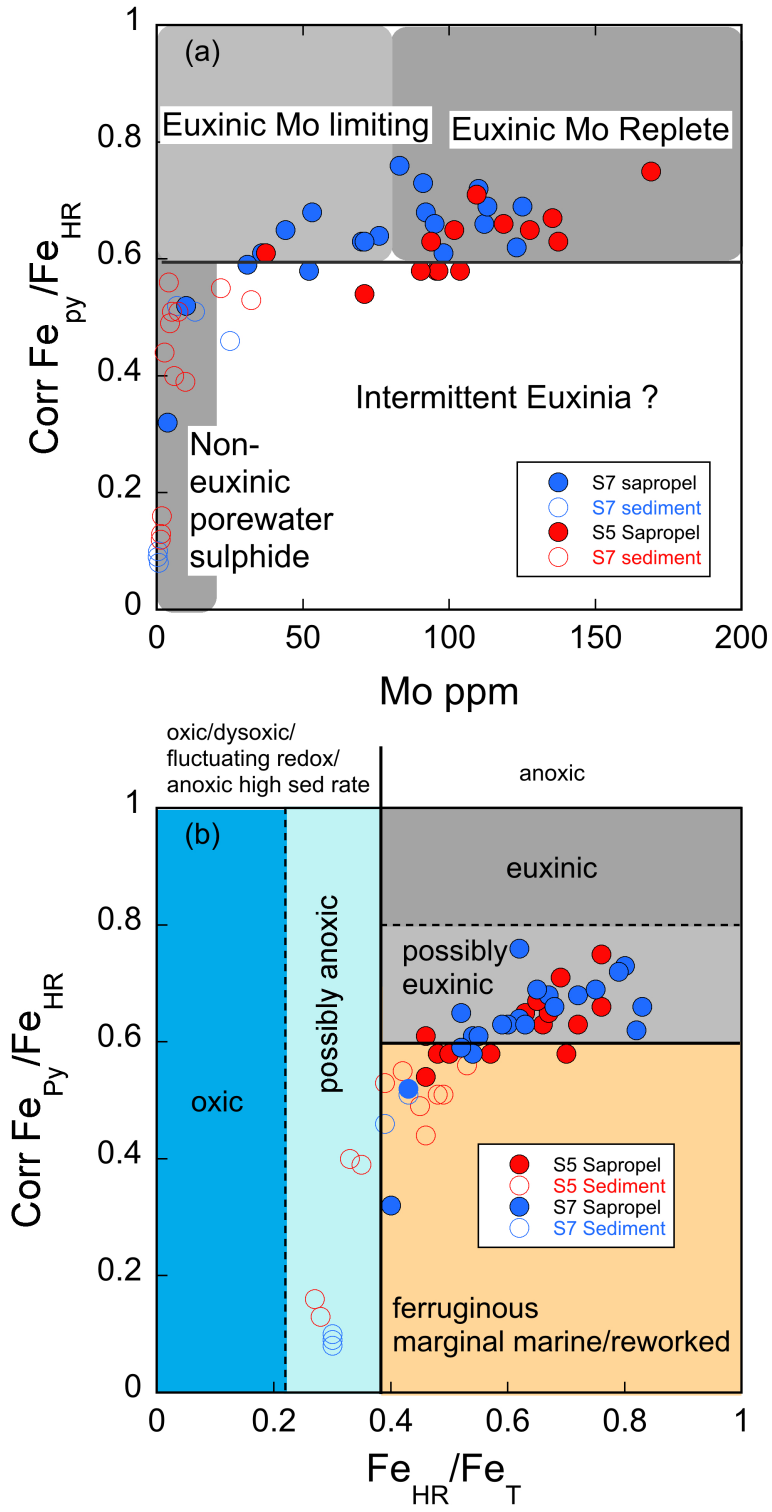
(a)
Euxinic Mo limiting
Euxinic Mo Replete
Intermittent Euxinia ?
Non-
euxinic
porewater
sulphide
S7 sapropel
S7 sediment
S5 Sapropel
S7 sediment
Corr Fe py /Fe HR
Mo ppm
0
0.2
0.4
0.6
0.8
1
0
50
100
150
200
oxic/dysoxic/
fluctuating redox/
anoxic high sed rate
anoxic
(b)
euxinic
possibly
euxinic
possibly anoxic
oxic
ferruginous
marginal marine/reworked
S5 Sapropel
S5 Sediment
S7 Sapropel
S7 Sediment
Corr Fe Py /Fe HR
Fe HR /Fe T
0
0.2
0.4
0.6
0.8
1

Figure 9

Table 1 Sample, elemental and isotopic data

Sample No	Mean depth	Fe/Al	Ba/Al	Mn/Al	Ni/Al	U/Al	V/Al	Mo/Al	UEF	MoEF	δ^{56}Fe (‰)	Error
	(cm)	g/g	g/g*10^4	g/g*10^4	g/g*10^4	g/g*10^4	g/g*10^4	g/g*10^4			IRMM-14	2σ (n)
Sapropel S5 (ODP967C-1H5)												
1H5 51-52	51.5	0.69	22	117	10.1	0.5	18.5	0.2	4.8	1.5	0.22	0.09(4)
1H5 56-57	56.5	0.70	16	72	8.1	0.5	14.1	0.1	4.3	1.1	0.17	0.09(8)
1H5 61-62	61.5	0.73	16	62	8.8	0.5	15.8	0.2	4.5	1.4	0.20	0.08(8)
1H5 66-67	66.5	0.67	18	63	9.2	0.7	17.7	0.8	6.4	7.1	0.11	0.10(4)
1H5 71-72	71.5	0.86	31	392	14.3	1.3	20.9	0.9	12.0	7.6	0.22	0.08(4)
1H5 76-77	76.5	1.05	104	149	22.0	4.3	62.7	15.8	40.1	133.1	-0.51	0.08(5)
1H5 78-79	78.5	1.20	220	244	33.0	7.6	109.6	32.0	70.8	269.3	-0.40	0.05(7)
1H5 80-81	80.5	1.17	179	244	30.1	7.2	98.2	24.1	66.9	202.6	-0.61	0.1 (5)
1H5 82-83	82.5	1.00	304	236	31.5	7.9	103.2	22.6	73.6	189.6	-0.29	0.10(13)
1H5 84-85	84.5	1.06	-	208	22.7	6.0	62.9	33.4	55.4	280.9	-0.27	0.07 (5)
1H5 86-87	86.5	1.02	210	231	29.6	9.9	91.6	26.0	160.6	218.3	-0.34	0.10(4)
1H5 88-89	88.5	0.98	-	184	26.2	7.0	62.4	26.1	65.2	219.5	-0.32	0.07(6)
1H5 90-91	90.5	0.99	190	201	26.5	7.1	53.2	30.2	65.5	253.4	-0.25	0.11(5)
1H5 92-93	92.5	1.30	245	170	28.6	6.7	54.5	37.9	61.6	318.9	-0.72	0.11(7)
1H5 94-95	94.5	0.80	136	195	19.6	3.9	45.0	12.2	36.4	102.5	0.04	0.03(3)
1H5 96-97	96.5	0.79	187	189	25.9	5.2	48.6	20.8	47.7	174.5	-0.01	0.10(5)
1H5 98-99	98.5	0.97	180	244	27.8	4.9	47.1	21.2	45.4	177.9	0.07	0.08(6)
1H5 100-101	100.5	0.89	91	178	24.9	3.1	52.4	18.3	28.2	153.6	-0.05	0.06(5)
1H5 102-103	102.5	0.99	38	575	20.4	1.6	41.2	6.6	14.7	55.8	-0.12	0.05(3)
1H5 104-105	104.5	0.79	18	129	11.7	0.9	18.1	4.0	8.3	33.4	-	
1H5 106-107	106.5	0.77	20	145	11.7	0.9	18.9	2.6	8.0	22.2	0.05	0.03(3)
1H5 111-112	111.5	0.75	42	327	18.2	1.0	20.4	0.9	9.7	7.9	0.20	0.03(3)
1H5 116-117	116.5	0.68	32	366	16.6	1.2	21.0	0.8	11.3	7.1	0.29	0.08(3)
1H5 121-122	121.5	0.66	28	511	12.9	1.4	18.0	0.5	12.5	3.9	0.51	0.07(3)
1H5 126-127	126.5	0.70	24	443	14.0	1.9	25.3	1.0	17.4	8.3	0.36	0.06(3)
1H5 131-132	131.5	0.65	27	379	19	0.7	20.8	1.5	6.6	12.8	0.15	0.07(3)
Sapropel S7 (ODP967-2H2,3)												
2H2-124-125	124.5	0.66	64	127	13.1	0.6	18.3	0.1	5.3	0.9	0.18	0.07(3)
2H2-129-130	129.5	0.63	63	206	13.8	1.0	19.1	0.0	9.1	0.4	0.10	0.07(3)
2H2 131-132	131.5	0.64	115	173	15.0	1.1	19.6	0.1	10.5	0.6	0.17	0.01(3)
2H2 133-134	133.5	0.71	204	201	24.1	2.2	36.1	0.8	20.3	6.4	0.05	0.05(3)
2H2134-135	134.5	0.78	256	197	31.9	2.8	54.9	2.1	25.9	17.8	-0.16	0.04(3)
2H2 135-136	135.5	0.97	309	206	46.8	4.9	73.5	8.2	45.0	68.7	-0.19	0.03(3)
2H2 136-137	136.5	1.01	315	216	50.3	5.4	73.7	11.5	50.1	96.4		
2H2 137-138	137.5	1.89	295	317	49.8	6.7	77.0	28.6	62.1	240.7	-0.44	0.10(3)
2H2 138-139	138.5	1.49	295	277	41.3	6.8	63.6	21.9	63.0	183.8	-0.57	0.023)
2H2 139-140	139.5	1.48	315	301	43.5	6.9	67.2	25.3	63.7	212.3	-0.64	0.01(3)
2H2 140-141	140.5	1.62	342	298	34.7	7.8	71.3	33.8	71.8	284.2	-0.72	0.02(3)
2H2 141-142	141.5	1.35	301	287	29.4	7.2	61.3	29.8	66.4	250.8	-0.55	0.03(3)
2H2 142-143	142.5	1.23	274	260	27.3	6.0	55.8	27.7	55.4	232.5	-0.54	0.03(6)
2H2 143-144	143.5	1.21	308	268	29.8	6.5	68.8	30.9	59.9	259.5	-0.41	0.06(3)
2H2 144-145	144.5	0.99	264	260	28.3	5.8	58.0	21.7	53.9	182.3	-0.27	0.00(3)
2H2 145-146	145.5	0.87	287	318	31.6	6.2	74.0	21.3	57.9	179.0	-0.14	0.03(3)
2H2 146-147	146.5	0.88	218	284	26.1	4.8	55.4	16.6	44.8	139.5	-0.09	0.03(3)
2H2 147-148	147.5	0.91	237	278	25.3	4.4	51.1	16.8	40.7	141.6	-0.06	0.02(3)
2H2 148-149	148.5	0.92	203	270	25.3	4.3	43.9	16.3	40.1	136.7	-0.09	0.19(9)
2H2 149-150	149.5	1.10	146	233	22.6	4.6	41.4	19.0	42.9	159.5	-0.42	0.07(3)
2H3 0-1	150.5	0.86	192	273	32.8	3.8	57.5	17.9	34.9	150.4	-0.06	0.05(3)
2H3 1-2	151.5	0.95	116	213	21.5	2.7	52.8	9.6	24.9	80.4	-0.09	0.08(3)
2H3 2-3	152.5	0.88	98	854	20.3	2.1	57.8	7.8	19.6	65.6	-0.10	0.03(3)
2H3 3-4	153.5	0.82	53	1914	15.0	1.5	37.3	5.0	13.8	42.2	-0.18	0.04(3)
2H3 5-6	155.5	0.76	26	167	10.5	1.2	21.4	3.1	11.3	25.7	0.18	0.09(6)
2H3 10-11	160.5	0.77	28	172	10.2	1.2	19.5	1.6	10.9	13.2	0.14	0.03(3)
2H3 15-16	165.5	0.79	33	177	10.5	1.0	20.5	0.9	9.1	7.7	0.02	0.07(3)

Mean Depth cm	% Fe detrital	Fe_T/Al	%Fe authigenic	$\delta^{56}Fe$ authigenic	Error
S5					
76.5	69	1.05	31	-2.00	0.13
78.5	60	1.20	40	-1.23	0.07
80.5	62	1.17	38	-1.85	0.14
82.5	72	1.00	28	-1.44	0.32
84.4	69	1.06	31	-1.19	0.16
86.5	71	1.02	29	-1.53	0.26
88.5	74	0.98	26	-1.63	0.21
90.5	73	0.99	27	-1.33	0.32
92.5	56	1.30	44	-1.82	0.09
98.5	75	0.97	25	-0.17	0.28
100.5	82	0.89	18	-0.93	0.38
102.5	80	0.91	20	-1.19	0.29
S7					
135.5	75	0.97	25	-1.21	0.11
136.5	71	1.01	29	-1.04	0.08
137.5	38	1.89	62	-0.81	0.04
138.5	49	1.49	51	-1.25	0.01
139.5	49	1.48	51	-1.39	0.01
140.5	45	1.62	55	-1.42	0.01
141.5	54	1.35	46	-1.36	0.03
142.5	59	1.23	41	-1.52	0.04
143.5	60	1.21	40	-1.24	0.08
144.5	73	0.99	27	-1.41	0.00
145.5	83	0.87	17	-1.59	0.35
146.5	82	0.88	18	-1.18	0.24
147.5	79	0.91	21	-0.87	0.12
149.5	66	1.10	34	-1.51	0.12
150.5	84	0.86	16	-1.12	0.43
151.5	76	0.95	24	-0.86	0.28
152.5	83	0.88	17	-1.29	0.20